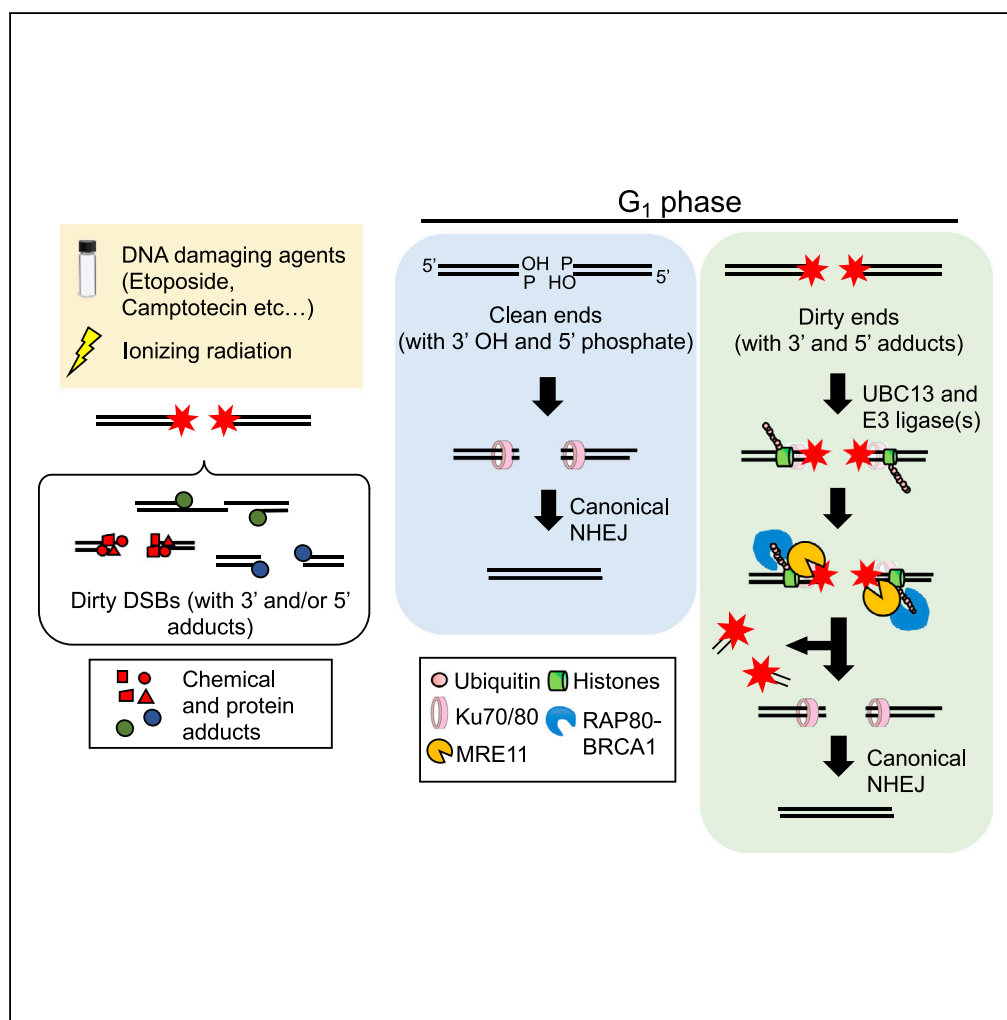**Article**

UBC13-Mediated Ubiquitin Signaling Promotes Removal of Blocking Adducts from DNA Double-Strand Breaks

Remi Akagawa,
Hai Thanh Trinh,
Liton Kumar
Saha, ..., Shinichiro
Nakada, Shunichi
Takeda, Hiroyuki
Sasanuma

stakeda@rg.med.kyoto-u.ac.jp
(S.T.)
hiroysasa@rg.med.kyoto-u.ac.
jp (H.S.)

HIGHLIGHTS

We establish a bioassay to
identify the proteins that
remove blocking adducts

UBC13 facilitates the
removal of blocking
adducts by recruiting
MRE11 to DSB sites

UBC13 and RAP80 are
required for BRCA1-
MRE11 interaction in G_1
phase

The UBC13-BRCA1-
MRE11 axis functions
independently of TDP2

Article

UBC13-Mediated Ubiquitin Signaling Promotes Removal of Blocking Adducts from DNA Double-Strand Breaks

Remi Akagawa,[1] Hai Thanh Trinh,[1] Liton Kumar Saha,[1,7] Masataka Tsuda,[1,8] Kouji Hirota,[2] Shintaro Yamada,[1,3] Atsushi Shibata,[4] Masato T. Kanemaki,[5] Shinichiro Nakada,[6] Shunichi Takeda,[1,*] and Hiroyuki Sasanuma[1,9,*]

SUMMARY

Chemical modifications and adducts at DNA double-strand break (DSB) ends must be cleaned before re-joining by non-homologous end-joining (NHEJ). MRE11 nuclease is essential for efficient removal of Topoisomerase II (TOP2)-DNA adducts from TOP2 poison-induced DSBs. However, mechanisms in MRE11 recruitment to DSB sites in G_1 phase remain poorly understood. Here, we report that TOP2-DNA adducts are expeditiously removed through UBC13-mediated polyubiquitination, which promotes DSB resection in G_2 phase. We found that this ubiquitin signaling is required for efficient recruitment of MRE11 onto DSB sites in G_1 by facilitating localization of RAP80 and BRCA1 to DSB sites and complex formation between BRCA1 and MRE11 at DSB sites. UBC13 and MRE11 are dispensable for restriction-enzyme-induced "clean" DSBs repair but responsible for over 50% and 70% of NHEJ-dependent repair of γ-ray-induced "dirty" DSBs, respectively. In conclusion, ubiquitin signaling promotes nucleolytic removal of DSB blocking adducts by MRE11 before NHEJ.

INTRODUCTION

A DNA double-strand break (DSB) is the most genotoxic type of DNA lesion. If misrepaired or left unrepaired, DSBs can lead to carcinogenesis and cell death. DSBs are repaired by two major repair pathways: homology-directed repair (HDR) and non-homologous end joining (NHEJ) (O'Driscoll and Jeggo, 2006). HDR is active only in the S/G_2 phases, whereas NHEJ functions throughout the cell cycle (Moynahan and Jasin, 2010) (Chang et al., 2017) (Nickoloff et al., 2017) (Shrivastav et al., 2008). Note that NHEJ plays the dominant role in the G_0/G_1 phases and repairs approximately 80% of ionizing-radiation (IR)-induced DSBs even in the S/G_2 phases (Beucher et al., 2009) (Shibata et al., 2014). NHEJ is initiated by the binding of a KU70/KU80 heterodimer and a DNA-PK-dependent protein kinase catalytic subunit (DNA-PKcs) to the DSB ends and finishes with ligation by a complex involving DNA LIGASE 4 (LIG4) and XRCC4 (Chang et al., 2017) (Dynan and Yoo, 1998). Ligation by LIG4 requires 3'-OH and 5'-phosphate DSB ends, termed "clean" DSBs (Robins and Lindahl, 1996) (Chappell et al., 2002). Thus, direct ligation by NHEJ requires the prior removal of blocking adducts and the restoration of ligatable (clean) DSB ends.

DSBs induced by endogenous and exogenous sources are generally accompanied by chemical adducts at DSB ends and are termed "dirty" DSBs (Asaithamby et al., 2011) (Woodbine et al., 2011). A typical exogenous source, IR, generates such dirty DSBs bearing multiple DNA lesions, including abasic sites and damaged bases at DSB ends (Davis and Chen, 2014) (Schipler and Iliakis, 2013) (Averbeck et al., 2014) (Jeggo et al., 2011) (Mladenov et al., 2018). Dirty DSBs are also produced by an anti-cancer Topoisomerase II (TOP2) poison, etoposide, which stabilizes the covalent association of TOP2 adducts at the 5' ends of DSBs, referred to as a pathological TOP2 cleavage complex (TOP2cc) and also TOP2-DNA adducts (Pommier et al., 2016). Since chemical modifications as well as 5' TOP2 adducts obstruct direct ligation of ends by LIG4, these blocking adducts need to be removed prior to ligation by NHEJ. Removal of such blocking modifications from DSBs is the rate-limiting step in DSB repair. This is evidenced by data showing that the vast majority of restriction-enzyme (RE) (AsiSI)-induced ligatable clean DSBs are repaired within an hour (Caron et al., 2015), whereas it takes several hours for DSB-repair pathways to ligate the majority of dirty DSBs induced by IR and etoposide (Hoa et al., 2016; Woodbine et al., 2014). However, the molecular mechanisms underlying the removal of the blocking adducts remains poorly understood, in part owing to the complexity of blocking adducts present at IR-induced DSBs.

[1]Department of Radiation Genetics, Graduate School of Medicine, Kyoto University, Yoshida Konoe, Sakyo-ku, Kyoto 606-8501, Japan

[2]Department of Chemistry, Graduate School of Science, Tokyo Metropolitan University, Hachioji-shi, Tokyo 192-0397, Japan

[3]Molecular Biology Program, Memorial Sloan Kettering Cancer Center, New York, NY 10065, USA

[4]Signal Transduction Program, Gunma University Initiative for Advanced Research (GIAR), Gunma University, Maebashi, Gunma 371-8511, Japan

[5]National Institute of Genetics, Research Organization of Information and Systems (ROIS), and Department of Genetics, The Graduate University for Advanced Studies (SOKENDAI), Yata 1111, Mishima, Shizuoka 411-8540, Japan

[6]Department of Bioregulation and Cellular Response, Graduate School of Medicine, Osaka University, Suita, Osaka 565-0871, Japan

[7]Present address: Developmental Therapeutics Branch and Laboratory of Molecular Pharmacology, Center for Cancer Research, National Cancer Institute, NIH, Bethesda, MD 20892, USA

[8]Present address: Department of Mathematical and Life Sciences, Graduate School of Science, Hiroshima University, Hiroshima 739-8526, Japan

[9]Lead Contact

*Correspondence:
stakeda@rg.med.kyoto-u.ac.jp (S.T.),
hiroysasa@rg.med.kyoto-u.ac.jp (H.S.)

https://doi.org/10.1016/j.isci.2020.101027

MRE11 forms a complex with RAD50 and NBS1 (Xrs2 in *Saccharomyces cerevisiae*), and the resulting MRN(X) complex is involved in the initial DSB resection step of HDR, which generates 3′ single-stranded tails at DSBs (Shibata et al., 2014) (Roques et al., 2009) (Mimitou and Symington, 2008; Zhu et al., 2008) (Garcia et al., 2011) (reviewed in Oh and Symington, 2018; Paull, 2018). Yeast genetic studies suggest an important role for MRE11 endonuclease in the repair of DSBs with dirty ends as evidenced by the following study. Although *Saccharomyces cerevisiae* mutants expressing nuclease-deficient MRE11 perform HDR of RE-induced clean DSBs with nearly normal kinetics, the mutant is extremely sensitive to IR (Oh and Symington, 2018) (Moreau et al., 1999) (Westmoreland and Resnick, 2013), suggesting that MRE11 plays an important role in DSB repair other than DSB resection, potentially by removing blocking adducts. This is supported by data showing that the nuclease activity of *Schizosaccharomyces pombe* MRE11 removes both 3′ TOP1 and 5′ TOP2 adducts from DSBs *in vivo* (Hartsuiker et al., 2009). Moreover, the nuclease activity of purified MRN complex is capable of removing both 3′ and 5′ blocking adducts from DSBs (Cannavo and Cejka, 2014) (Deshpande et al., 2016) (Deshpande et al., 2018) (reviewed in (Paull, 2018)). Although the role of yeast MRE11 in creating ligatable ends has been established by comparing the repair kinetics of IR-induced dirty DSBs with those of RE-induced clean DSBs (Lisby et al., 2004; Westmoreland and Resnick, 2013), similar studies have not yet been performed in mammalian cells, because human cells deficient in MRE11 nuclease activity display severe genome instability and are inviable (Hoa et al., 2016).

The removal of blocking TOP2 adducts provides an excellent way to examine the molecular mechanism by which dirty DSBs are processed and clean DSBs are restored for the following reasons. Pulse exposure to etoposide specifically generates DSBs bearing a well-characterized blocking adduct, a pathological TOP2cc, and its number can be accurately measured (Hoa et al., 2016). TOP2 normally resolves DNA catenanes by transiently forming a DSB, a TOP2cc in duplex DNA, which allows the intact DNA duplex to pass through the DSB, followed by religation of the DSB by TOP2 (Cowell and Austin, 2012) (Nitiss, 2009). The repair of etoposide-induced DSBs is performed by NHEJ as well as by HDR (Hoa et al., 2016) (Aparicio et al., 2016). Repair by NHEJ requires prior removal of 5′ TOP2 adducts by tyrosyl-DNA-phosphodiesterase 2 (TDP2) and MRE11 (Hoa et al., 2016) (Ledesma et al., 2009) (Lee et al., 2018). MRE11 contributes to the removal of 5′ TOP2 adducts to a considerably greater extent than does TDP2, as MRE11 nuclease-deficient cells, but not $TDP2^{-/-}$ cells, display an endogenous accumulation of pathological TOP2ccs, which leads to cell death (Hoa et al., 2016). In HDR, MRE11 nuclease activity is tightly controlled by the ubiquitination and phosphorylation pathways during DSB resection in the S/G_2 phases (Jachimowicz et al., 2019) (Dong et al., 1999) (Costanzo et al., 2001) (Falck et al., 2012) (Kijas et al., 2015). It remains unclear exactly how MRE11 nuclease is activated at pathological TOP2ccs during the G_1 phase.

The E3 ligase RNF168 catalyzes H2A K15 monoubiquitination and K63-linked polyubiquitination near DSB sites (Kolas et al., 2007) (Huen et al., 2008) (Stewart et al., 2009) (Doil et al., 2009) (Mattiroli et al., 2012) (Uckelmann and Sixma, 2017). UBC13 plays a crucial role in K63-linked polyubiquitination (Stewart et al., 2009) (Mattiroli et al., 2012) (Zhao et al., 2007). RAP80 is a reader of K63-linked ubiquitin chains and facilitates the recruitment of the BRCA1-A complex onto DSB sites (Sato et al., 2009) (Wang et al., 2007) (Kim et al., 2007) (Sobhian et al., 2007) (Hu et al., 2011). The induction of DSBs leads to the formation of a complex between BRCA1 and MRE11 at DSB sites in a UBC13-dependent manner and promotes DSB resection (Zhao et al., 2007) (Greenberg et al., 2006) (Chen et al., 2008). RNF168 and BRCA1 play a redundant role in promoting HDR (Zong et al., 2019). It remains unclear whether UBC13-dependent K63 ubiquitin signaling also contributes to DSB repair during the G_1 phase (reviewed in Nakada, 2016; Uckelmann and Sixma, 2017). Although NHEJ is required for both V(D)J recombination of antigen receptor genes and development of B and T lymphocytes (Alt et al., 2013), V(D)J recombination is not impaired by the loss of MRE11, RAP80, RNF168, or UBC13, indicating that all four are dispensable for NHEJ of clean DSBs carrying 3′-OH and 5′-phosphate moieties (Yamamoto et al., 2006) (Bohgaki et al., 2011) (Yin et al., 2012) (Dinkelmann et al., 2009).

To date, no bioassay has accurately assessed the capability of NHEJ except analysis of V(D)J recombination. Previous studies have evaluated the efficiency of NHEJ by measuring the repair kinetics of IR-induced DSBs as well as IR sensitivity in the G_1 phase. However, these phenotypic assays do not distinguish NHEJ from the preceding step, which involves the processing of dirty DSBs to restore clean ends. Another widely used phenotypic analysis of NHEJ measures the repair of I-*Sce*1 RE-induced DSBs in reporter genes (reviewed in Jasin and Haber, 2016). However, this assay does not assess the frequency of the accurate DSB-repair events that restore the I-*Sce*1 site, even though the vast majority of the NHEJ events are accurate (Bétermier et al., 2014). Here we describe a new assay for assessing the capability of NHEJ. To this end,

we expressed a regulatable *Asi*SI RE coupled to the estrogen receptor (ER-*Asi*SI) in cells (Caron et al., 2015) (Aymard et al., 2014); pulse-exposed the cells to an estrogen antagonist, 4-hydroxytamoxifen (4-OHT), to transiently activate *Asi*SI; and measured the number of unrepaired DSBs during the G_1 phase. We verified over a 100-fold delay in DSB repair in the absence of LIG4. We, therefore, conclude that our repair kinetics analysis of ER-*Asi*SI-induced DSBs may measure virtually all NHEJ events in *wild-type* cells.

We show that UBC13 promotes the recruitment of MRE11 nuclease to remove 5′ TOP2 adducts from pathological TOP2ccs for subsequent NHEJ. We tested the involvement of UBC13 and MRE11 nuclease activity in the repair of IR-induced DSBs in the G_1 phase. Although both these factors are essential for the efficient repair of dirty DSBs generated by etoposide and IR, they are both dispensable for the repair of *Asi*SI-induced clean DSBs. These results indicate that the UBC13 promotes MRE11-dependent removal of blocking adducts from IR-induced dirty DSBs in addition of that of TOP2 adducts prior to their ligation by NHEJ. We propose that K63-linked ubiquitin signaling involving MRE11 is indicated as the key step to determine the repair kinetics of dirty DSBs.

RESULTS

UBC13 Contributes to DSB Repair during the G_1 Phase

We exposed an asynchronous population of MCF-7 human breast cancer cells to etoposide for 30 min, then counted the number of conjugated-ubiquitin FK2 foci, which represent various types of ubiquitin chains (Shi et al., 2008). Table S1 shows the list of mutant cells analyzed in this study. We detected FK2 foci colocalizing with 53BP1 foci in virtually all cells (Figure S1A). We also detected etoposide-induced FK2 foci in serum-starved G_1 cells (Figures S1A and S1B). We depleted UBC13 with shRNA (shUBC13) in the serum-starved cells (Figure S1C) and found an ~80% decrease in the number of etoposide-induced FK2 foci (Figures 1A, S1A, and S1D). Since UBC13 promotes K63-linked polyubiquitination at DSB sites (Stewart et al., 2009), this result indicates that a majority of the FK2 foci contain K63-linked polyubiquitination. We found that UBC13 depletion impaired H2AX ubiquitination in G_1 phase, suggesting that H2AX is one of the targets of UBC13 (Figure S1E). Thus, UBC13 generates K63-linked polyubiquitin chains of the substrates, including H2A/H2AX, at DSB sites in the G_1 as well as in the S/G_2 phases.

To confirm the role of UBC13 in DSB repair in the G_1 phase, we exposed serum-starved MCF-7 cells to etoposide for 30 min, then monitored the resolution kinetics of the γH2AX foci (Figures 1B and S1F). Pulse exposure (0.5 h) to etoposide caused similar increases in the number of γH2AX foci in all cell types tested. At 8 h after removal of etoposide, the number of γH2AX foci had diminished almost to background levels in the control cells but persisted in the *DNA-PKcs$^{-/-}$* mutant cells (Figures 1B and S1F–S1H). The delay in DSB repair in the shUBC13 cells was also more prominent than in the control cells. These results suggest that UBC13 contributes to DSB repair through a pathway other than HDR. We next assessed the possible functional interaction between UBC13 and canonical NHEJ by depleting UBC13 in *DNA-PKcs$^{-/-}$* cells (Figure S1C) and examining the etoposide-induced γH2AX foci. The depletion of UBC13 did not affect the repair kinetics of *DNA-PKcs$^{-/-}$* cells (Figures 1B and S1F). Since UBC13 is dispensable for efficient NHEJ (Yamamoto et al., 2006), it is surprising that UBC13 shows a phenotype similar to DNA-PKcs deficiency for the repair of TOP2cc lesions caused by etoposide. Moreover, this epistatic relationship between UBC13 and NHEJ suggests that UBC13 contributes to NHEJ-mediated repair of these lesions.

UBC13-Dependent Focus Formation of BRCA1 and RAP80 in G_1 Cells

UBC13-dependent ubiquitination promotes the recruitment of various factors, including BRCA1 and RAP80, to DSB sites in the S/G_2 phases (reviewed in Nakada, 2016; Uckelmann and Sixma, 2017). We asked whether the formation of BRCA1 and RAP80 foci could also occur in the G_1 phase. Pulse exposure (0.5 h) to etoposide caused 2.9- and 2.4-fold increases in the number of BRCA1 and RAP80 foci, respectively, in serum-starved *wild-type* MCF-7 cells (Figures 1C, 1D, S1I, and S1J). UBC13 depletion reduced the numbers of BRCA1 foci and RAP80 foci by 5 and 1.5 folds, respectively, in G_1 cells. Additionally, the truncated form of RAP80 lacking ubiquitin-interacting motifs (RAP80-UIMΔ), which specifically recognize K63-linked polyubiquitin chains of H2A/H2AX (Figures S1K and S1L) (Mattiroli et al., 2012; Sato et al., 2009), completely abolished the ability to form foci after etoposide treatment in G_1 phase. These results indicate that, similar to what has been observed during the S/G_2 phases (Wang and Elledge, 2007), UBC13-dependent K63-linked ubiquitination plays a pivotal role in the recruitment of BRCA1 and RAP80 onto DSB sites during the G_1 phase.
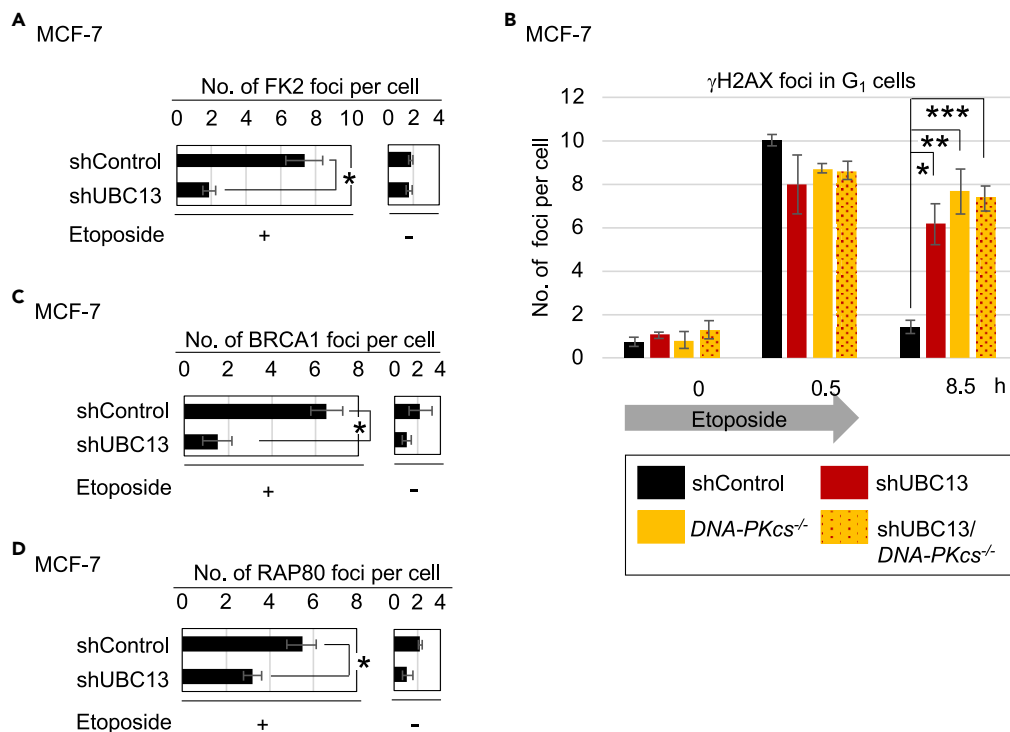
Figure 1. UBC13 Contributes to DSB Repair by Recruiting BRCA1 and RAP80 onto DSB Sites during the G_1 Phase

(A) Average number of etoposide-induced FK2 foci in MCF-7 cells synchronized during the G_1 phase by serum starvation (24 h). We examined *wild-type* MCF-7 cells treated with shRNA targeting UBC13 (shUBC13) and non-targeting shRNA (shControl). Synchronized cells were treated with etoposide (10 μM) for 30 min, washed, and incubated with etoposide-free media. Error bars show the standard deviation (SD) from three independent experiments. At least 50 G_1-phase (cyclin A-negative) cells per experiment were counted. Single asterisk indicates $p = 1.1 \times 10^{-3}$, calculated by Student's t test. Representative images and box plots of FK2 foci are shown in Figures S1A and S1D, respectively.

(B) DSB-repair kinetics of G_1-phase MCF-7 cells after pulse exposure (0–0.5 h) to etoposide (10 μM). Average number of γH2AX foci was counted at 0.5 and 8.5 h after addition of etoposide. Data are as shown in (A). Single, double, and triple asterisks indicate $p = 1.2 \times 10^{-3}$, $p = 5.6 \times 10^{-4}$, and $p = 3.2 \times 10^{-5}$, respectively, calculated by Student's t test. The box plots of γH2AX foci are shown in Figure S1F.

(C and D) Average number of etoposide-induced BRCA1 (C) and RAP80 (D) foci per cell. The experimental procedure and data are as shown in (A). Asterisks indicate $p = 9.3 \times 10^{-4}$ in (C) and $p = 8.0 \times 10^{-3}$ in (D). Representative images and box plots of BRCA1 and RAP80 foci are shown in Figures S1I and S1J, respectively.

RAP80 and BRCA1 Contribute to DSB Repair during G_1 Phase

To test the role of RAP80 in DSB repair in the G_1 phase, we generated $RAP80^{-/-}$ cells by disrupting exon 5 of $RAP80$ in TK6 human B cells and in MCF-7 cells (Figures S2A and S2B). NHEJ is preferred over HDR to repair etoposide-induced DSBs (Maede et al., 2014). The $RAP80^{-/-}$ cells showed a higher sensitivity to etoposide than did the *wild-type* cells (Figures S2C and S2D). To analyze the role of RAP80 in DSB repair in the G_1 phase, we enriched G_1-phase MCF-7 cells by serum starvation, exposed the cells to etoposide for 30 min, then monitored the resolution kinetics of the γH2AX foci (Figures 2A and S2E). Remarkably, the NHEJ-deficient $DNA\text{-}PKcs^{-/-}$ and the $RAP80^{-/-}$ MCF-7 cells exhibited a very similar phenotype: a strong defect in the repair of etoposide-induced DSBs (Figures 2A and S2E). Thus, RAP80 plays an important role in NHEJ-dependent repair of etoposide-induced DSBs in the G_1 phase. Since RAP80 is dispensable for NHEJ of clean DSBs (Yin et al., 2012), our results suggest that RAP80 is involved in the repair of DSBs with TOP2 adducts, similar to BRCA1 (Sasanuma et al., 2018).

We next investigated the impact of $RAP80$ disruption on BRCA1-focus formation at etoposide-induced DSB sites in serum-starved G_1 MCF-7 cells. The loss of RAP80 caused a 20-fold decrease in the number of etoposide-induced BRCA1 foci (Figures 2B and S2F), indicating that RAP80 is required for the recruitment of BRCA1 onto DSB sites in the G_1 phase. We previously showed that BRCA1 plays an
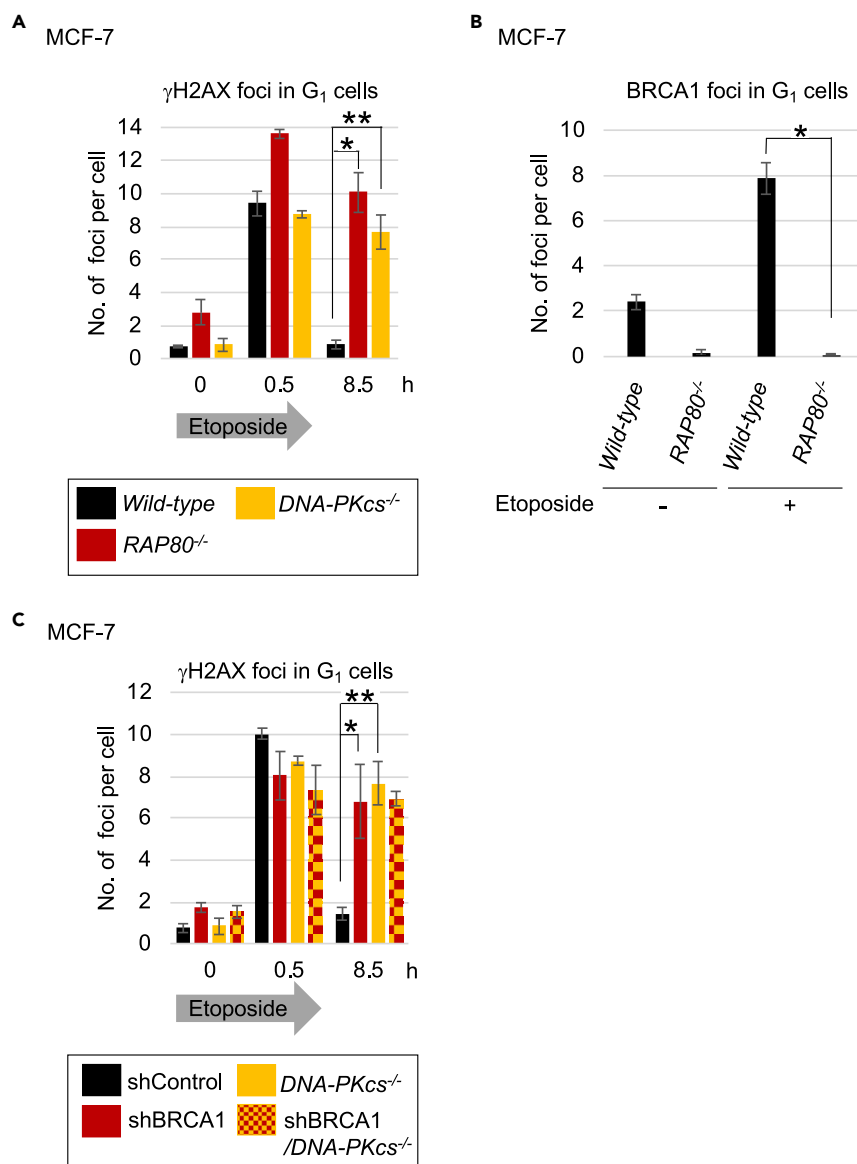
Figure 2. RAP80 and BRCA1 Contribute to DSB Repair during the G_1 Phase

(A) Analysis of DSB-repair kinetics (as presented in Figure 1B). Single and double asterisks indicate p = 1.3 × 10^{-4} and p = 3.8 × 10^{-4}, respectively. Representative images and box plots of γH2AX foci are shown in Figure S2E.

(B) Average number of etoposide-induced BRCA1 foci in *wild-type* and *RAP80$^{-/-}$* MCF-7 cells before and after pulse exposure (0.5 h) to etoposide. Standard deviation (SD) was calculated from three independent experiments. Asterisk indicates p = 4.3 × 10^{-5}. Representative images and box plots of BRCA1 foci are shown in Figure S2F.

(C) DSB-repair kinetics of MCF-7 cells in the G_1 phase following pulse exposure (0.5 h) to etoposide (10 μM). Experimental procedure and data presentation are as shown in Figure 1B. Single and double asterisks indicate p = 6.5 × 10^{-3} and p = 3.2 × 10^{-5}, respectively. Representative images and box plots of γH2AX foci are shown in Figure S2H.

important role in the removal of 5′ TOP2 adducts from pathological TOP2ccs in the G_1 phase (Sasanuma et al., 2018). In agreement with this, shRNA-mediated depletion of BRCA1 (Figure S2G) delayed the repair kinetics of etoposide-induced DSBs in *wild-type* cells to a level very similar to that found in *DNA-PKcs$^{-/-}$* cells (Figures 2C and S2H). The depletion did not further delay repair kinetics in *DNA-PKcs$^{-/-}$* cells (Figures 2C and S2H). Thus, both UBC13 and RAP80 play a crucial role in the NHEJ-mediated repair of etoposide-induced DSBs, most likely by recruiting BRCA1 onto DSB sites and promoting the removal of 5′ TOP2 adducts from DSBs.
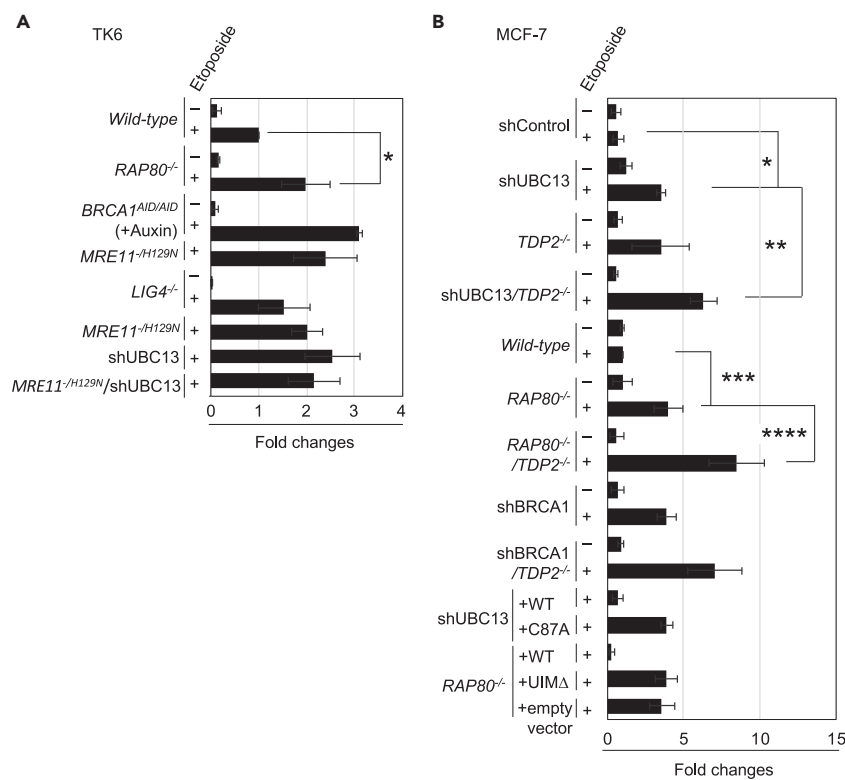
Figure 3. UBC13, RAP80, and BRCA1 Promote the Removal of Etoposide-Induced TOP2 Adducts Independent of TDP2

(A) Quantification of TOP2-DNA-cleavage-complexes (TOP2ccs) in TK6 lymphoid cells carrying the indicated genotypes relative to the amount of TOP2ccs in *wild-type* cells. Schematic of *in vivo* TOP2cc measurement by immunodetection with α-TOP2 antibody is shown in Figure S3A. Cells were treated with etoposide (10 μM) ("+") or DMSO ("-") for 2 h. BRCA1$^{AID/AID}$ cells were pretreated with auxin for 2 h, then incubated with etoposide (10 μM) plus auxin for an additional 2 h. MRE11$^{+/H129N}$ cells were treated with 4-hydroxytamoxifen (4-OHT) for 3 days to inactivate the *wild-type* MRE11 allele, then treated with etoposide (10μM) for 2 h. Error bars represent standard deviation (SD) of three independent experiments. Asterisk indicates p = 2.8 × 10^{-2}, calculated by Student's t test. Representative images of dot plots are shown in Figure S3E.

(B) Quantification of TOP2ccs in MCF-7 cells with the indicated genotypes relative to the amount of TOP2ccs in *wild-type* MCF-7 cells. Cells were incubated with serum-free medium for 24 h then treated with etoposide for 2 h. Each experiment was performed independently at least three times. Error bars represent SD. Single, double, triple, and quadruple asterisks indicate p = 4.7 × 10^{-4}, p = 6.4 × 10^{-3}, p = 5.3 × 10^{-3}, and p = 1.9 × 10^{-2} respectively, calculated by Student's t -test. Representative images of dot plots are shown in Figures S3F and S3G.

UBC13, RAP80, and BRCA1 Promote the Removal of Etoposide-Induced TOP2 Adducts Independent of TDP2

We measured the number of TOP2ccs in the G$_1$ phase by analyzing serum-starved MCF-7 cells. We lysed cells and separated TOP2cc from free TOP2 in cellular lysates by subjecting them to sedimentation by means of cesium chloride (CsCl) density-gradient ultra-centrifugation, as described previously (Hoa et al., 2016). TOP2ccs were detected as single or double dots in the middle fractions of the TOP2-DNA complex, shown at the bottom of the blot in Figure S3A. As demonstrated previously, we detected a greater number of etoposide-induced TOP2ccs in both nuclease-deficient MRE11$^{-/H129N}$ and BRCA1-depleted TK6 cells, compared with *wild-type* cells (Hoa et al., 2016) (Sasanuma et al., 2018) (Figures 3A, S3B, and S3E). To identify the role played by UBC13 in removing etoposide-induced TOP2ccs, we depleted UBC13 in serum-starved MCF-7 cells and subjected these cells to the same assay. The MCF-7 cells also showed a greater number of TOP2ccs (Figures 3B and S3F) compared with shControl cells. UBC13-depleted cells reconstituted with *wild-type* UBC13 (shUBC13-WT) did not accumulate etoposide-induced TOP2ccs, whereas expression of catalytically inactive UBC13 C87A mutant protein (shUBC13-C87A) re-sulted in accumulation of TOP2ccs compared with that of shUBC13 cells (Figures 3B, S3D, and S3F). These

results indicate that E2 ubiquitin-conjugating activity of UBC13 is required for the efficient removal of 5′ TOP2 adducts. Likewise, $RAP80^{-/-}$ cells and $RAP80^{-/-}$ cells expressing RAP80-UIMΔ caused an increase in the number of TOP2ccs in serum-starved MCF-7 cells (Figures 3B and S3G). We therefore conclude that ubiquitin signaling pathway involving BRCA1, RAP80, and UBC13 is required for efficient removal of 5′ TOP2 adducts from etoposide-induced TOP2ccs.

Since TDP2 is implicated in removal of TOP2ccs (Ledesma et al., 2009) we tested if UBC13 and RAP80 facilitate the removal of 5′ TOP2 adducts in a manner dependent on TDP2. To this end, we depleted UBC13 and BRCA1 in $TDP2^{-/-}$ MCF-7 cells and generated $RAP80^{-/-}/TDP2^{-/-}$ MCF-7 cells (Figures S1C, S2B, and S2G), then measured the number of TOP2ccs in the G_1 phase. Consistent with earlier reports (Hoa et al., 2016) (Ledesma et al., 2009), depletion of TDP2 caused an increase in TOP2ccs upon etoposide treatment (Figures 3B and S3F). UBC13-depletion, $RAP80^{-/-}$ mutation, and BRCA1-depletion further enhanced the accumulation of etoposide-induced TOP2ccs in $TDP2^{-/-}$ cells (Figures 3B, S3F, and S3G). Thus, like BRCA1, UBC13 and RAP80 promote the removal of 5′ TOP2 adducts in a TDP2-independent manner in the G_1 phase.

To examine the genetic interaction between MRE11 and UBC13, we depleted UBC13 in $MRE11^{-/H129N}$ cells (shUBC13/$MRE11^{-/H129N}$) and analyzed etoposide-induced TOP2ccs. The accumulation of TOP2ccs in shUBC13/$MRE11^{-/H129N}$ cells is very similar to those of $MRE11^{-/H129N}$ cells (Figures 3A and S3E). This epistatic relationship suggests that UBC13-dependent ubiquitination pathway promotes the removal of TOP2ccs through MRE11 nuclease activity.

Ubiquitin Signaling Involving UBC13, RAP80, and BRCA1 Is Required for Efficient Recruitment of MRE11 Nuclease onto DSB Sites in G_1 Cells

We investigated the role played by UBC13-dependent ubiquitin signaling in the recruitment of MRE11 to DSB sites. To this end, we examined MRE11 foci following exposure of G_1-phase MCF-7 cells to etoposide. These treatments caused increases in the number of MRE11 foci colocalizing with 53BP1, a marker of DSB sites (Figure S4). MRE11-focus formation was impaired in BRCA1-depleted cells after etoposide treatment, as shown previously (Sasanuma et al., 2018) (Figure 4A). The depletion of UBC13 reduced the percentage of MRE11-positive cells by ~60% upon treatment with etoposide (Figures 4A and S4). Similarly, $RAP80^{-/-}$ cells showed an ~70% reduction in the percentage of MRE11-positive cells upon treatment with etoposide. These results indicate that in ubiquitin signaling involving UBC13, RAP80, and BRCA1, all three facilitate the recruitment of MRE11 onto DSB sites for the efficient removal of the adducts of dirty DSBs.

UBC13 Is Essential for DNA-Damage-Induced Stable Complex Formation between BRCA1 and MRE11 in the G_1 Phase

Upon DNA damage in the S/G_2 phases, BRCA1 physically interacted with the MRN complex (Greenberg et al., 2006; Polanowska et al., 2006) in a UBC13-dependent manner (Zhao et al., 2007), which promotes DSB resection by MRE11. This finding prompted us to analyze DNA-damage-induced complex formation between BRCA1 and MRE11, specifically in G_1-phase cells. We exposed serum-starved MCF-7 cells to etoposide for 30 min, immunoprecipitated BRCA1, and tested for the presence of co-immunoprecipitated MRE11 by western blotting. No interactions between BRCA1 and MRE11 were seen in the absence of etoposide, whereas etoposide exposure induced interactions (lanes 2 and 4 of Figure 4B). Remarkably, the depletion of UBC13 abolished the DNA-damage-induced interaction (lane 6 of Figure 4B). RAP80 deletion also decreased the amount of MRE11 associating with BRCA1 (lane 10 of Figure 4B). These results indicate that, upon DNA damage in the G_1 phase, UBC13 and RAP80 facilitate a stable interaction between BRCA1 and MRE11. These data support the notion that UBC13-mediated ubiquitin signaling activates the nuclease activity of MRE11 via interaction with BRCA1 at DSB sites. Considering the vital role played by UBC13, RAP80, and BRCA1 in NHEJ-dependent repair of etoposide-induced DSBs (Figures 1B, 2A, and 2C), these data suggest that UBC13-mediated ubiquitin signaling promotes the removal of 5′ TOP2 adducts by activating MRE11.

The Loss of LIG4 Reduces Repair of RE-Induced Clean DSBs over 100-Fold in the G_1 Phase

The I-Sce1 reporter assays currently used to measure NHEJ events do not correctly measure the capability of NHEJ, because the I-Sce1 RE can re-cleave the accurately repaired junction, introducing a bias in favor of inaccurate repair that deletes the I-Sce1 site (Bétermier et al., 2014). We thus sought to establish a method to measure the frequency of all NHEJ events correctly. To this end, we expressed ER-$AsiSI$ RE in TK6 cells
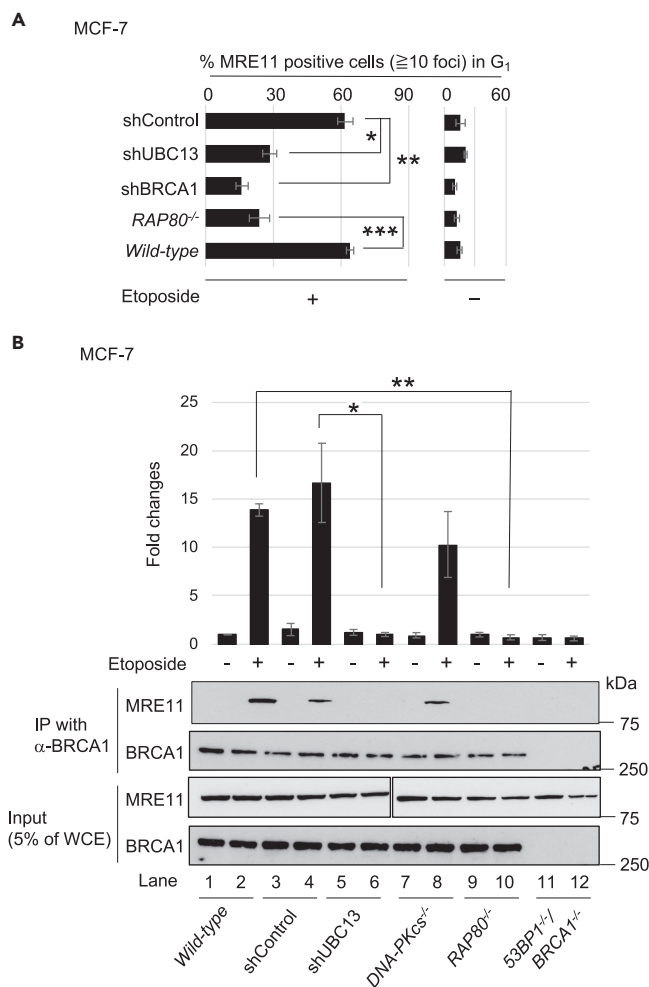
A MCF-7

B MCF-7

Figure 4. UBC13-Mediated Ubiquitin Signaling Involving UBC13, RAP80, and BRCA1 is Required for Efficient Recruitment of MRE11 Nuclease onto DSB Sites in G$_1$ Cells

(A) Quantification of MRE11-positive MCF-7 cells with at least 10 foci per nucleus for the indicated genotypes. Serum-starved MCF-7 cells were treated with etoposide (10 μM) for 30 min. Error bars were plotted for standard deviation (SD) from three independent experiments. Single, double, and triple asterisks indicate p = 2.3 × 10^{-4}, p = 5.3 × 10^{-5}, and p = 1.3 × 10^{-4}, respectively, calculated by Student's t test. Representative images of etoposide-induced MRE11/53BP1 foci are shown in Figure S4.

(B) Etoposide-induced complex formation of BRCA1 and MRE11 in G$_1$-phase MCF-7 cells. Whole-cell extracts (WCEs) were prepared from the indicated cells, untreated ("-") or treated ("+") with etoposide (10 μM) for 0.5 h. "Input" indicates 5% of WCEs used for immunoprecipitation. BRCA1 was immunoprecipitated from the WCEs. Intensities of the immunoprecipitated MRE11 bands for the indicated genotypes were normalized to those of the input. The graph indicates relative band intensities of the MRE11 bands in comparison with the untreated wild-type (Lane 1). Single and double asterisks indicate p = 2.1 × 10^{-2} and p = 1.5 × 10^{-3}, respectively, calculated by Student's t test.

and introduced clean DSBs via pulse exposure (4 h) of cells to 4-OHT (Iacovoni et al., 2010). The 4-OHT treatment caused an increase by over eight times in the number of γH2AX foci in all genotypes (0 h in Figures 5A and S5A). The number of γH2AX foci did not decrease from 0 to 1 h after 4-OHT removal owing to residual cleavage activity of ER-AsiSI RE. From 1 to 2 h, the number of γH2AX foci had dropped almost to background levels in the wild-type cells (Figures 5A and S5A), which agrees with the previous finding that AsiSI-induced DSBs are repaired within an hour (Caron et al., 2015). In contrast, even at 4 h after 4-OHT removal, essentially all γH2AX foci persisted in the LIG4$^{-/-}$ cells, indicating that the AsiSI-induced DSBs are repaired through the NHEJ pathway. The data indicated over 100-fold delay in DSB repair in the absence of LIG4 (Figure 5A), which is in sharp contrast with only up to several folds decrease in the number of (inaccurate) NHEJ events measured by reporter genes carrying the I-Sce1 site in NHEJ-deficient cells in
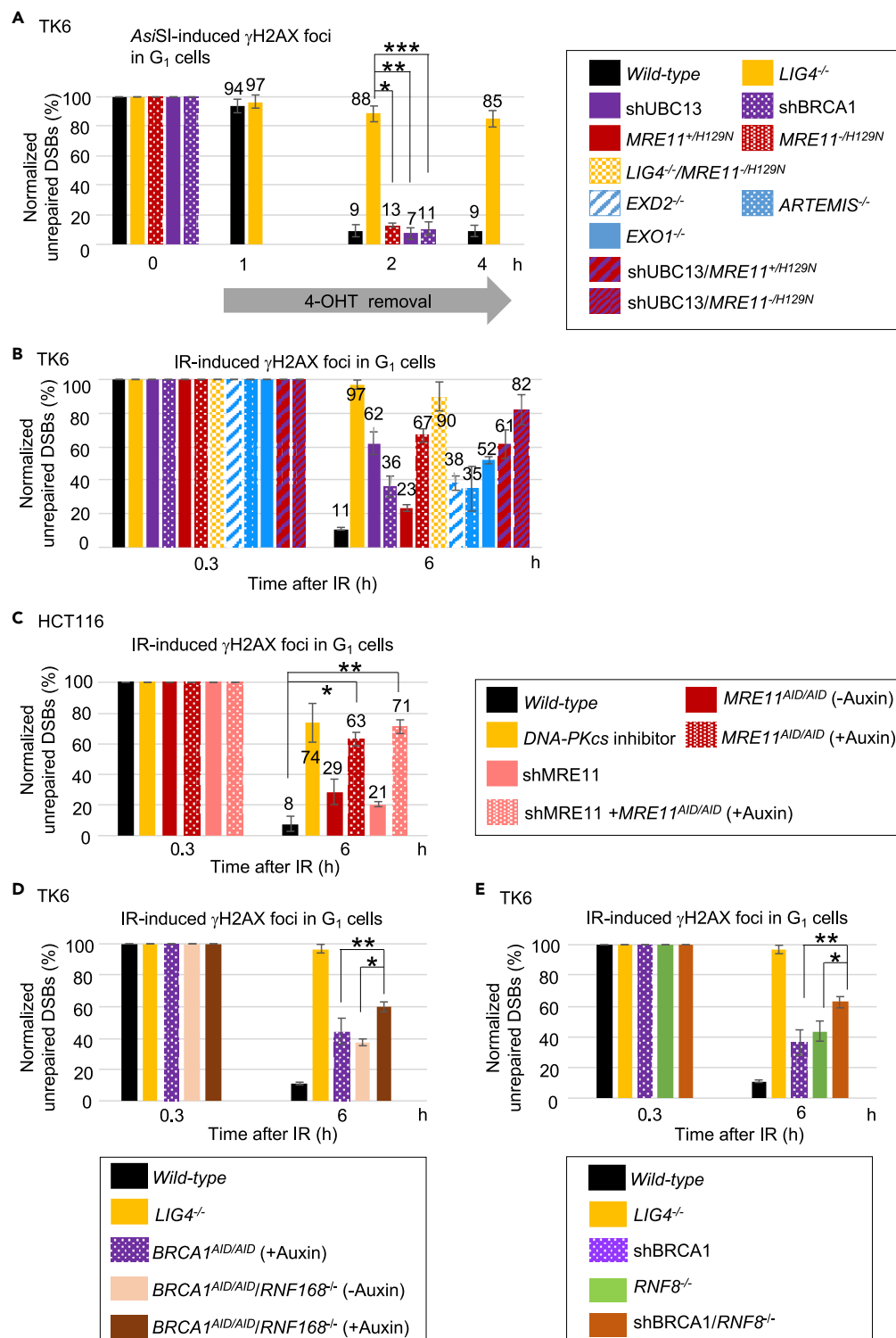
Figure 5. MRE11 Nuclease and UBC13-Mediated Ubiquitin Signaling Are Required for Efficient Repair of IR-Induced Dirty DSBs in the G$_1$ Phase

(A) Repair rate of DSBs induced by *Asi*SI restriction enzyme in G$_1$-phase TK6 cells. Cells expressing *Asi*SI fused with estrogen receptor (ER) were treated with 4-OHT for 4 h for DSB induction. We analyzed γH2AX foci in cyclin A-negative cells after 4-OHT was removed (time 0 h). We subtracted the average number of foci in the 4-OHT-untreated cells from the average number of foci in the 4-OHT-treated cells. Values correspond to the percentage of unrepaired DSBs relative to

Figure 5. *Continued*

the value at time 0 h, set to 100%. Error bars were plotted for standard deviation (SD) from three independent experiments. More than 50 G_1 cells (cyclin A negative) were analyzed for each experiment. Single, double, and triple asterisks indicate p = 1.9×10^{-5}, p = 2.9×10^{-5}, and p = 4.3×10^{-5}, respectively, calculated by Student's t test. Box plots of γH2AX foci at the indicated time points (0, 1, 2, and 4 h) are shown in Figure S5A.

(B–E) Repair rate of DSBs induced by IR (1 Gy) in G_1-phase TK6 and HCT116 cells. Average number of γH2AX foci in cyclin A-negative cells was counted at the indicated time points. We subtracted the average number of foci in IR-untreated cells from the average number of foci in IR-treated cells. Values correspond to the percentage of unrepaired DSBs relative to the value at time 0.3 h, set to 100%. Error bars were plotted for standard deviation (SD) from three independent experiments. In (B), p values were 2.0×10^{-4} (shUBC13 versus *wild-type*), 2.1×10^{-3} (shBRCA1 versus *wild-type*), 1.9×10^{-5} ($MRE11^{-/H129N}$ versus *wild-type*), 9.5×10^{-5} ($LIG4^{-/-}/MRE11^{-/H129N}$ versus *wild-type*), 4.1×10^{-4} ($EXD2^{-/-}$ versus *wild-type*), 3.6×10^{-2} ($ARTEMIS^{-/-}$ versus *wild-type*), 6.3×10^{-6} ($EXO1^{-/-}$ versus *wild-type*), and 1.7×10^{-4} (shUBC13/$MRE11^{-/H129N}$ versus *wild-type*), calculated by Student's t test. Box plots of γH2AX foci at the indicated time points (0, 0.3, and 6 h) are shown in Figure S5D. In (C), asterisks indicate p = 1.3×10^{-4} (single) and p = 7.9×10^{-5} (double), calculated by Student's t test. Box plots of γH2AX foci at the indicated time points (0, 0.3, and 6 h) are shown in Figure S6D. In (D), asterisks indicate p = 5.1×10^{-4} (single) and p = 3.8×10^{-2} (double), calculated by Student's t test. Box plots of γH2AX foci at the indicated time points (0, 0.3, and 6 h) are shown in Figure S5F. In (E), asterisks indicate p = 1.2×10^{-2} (single) and p = 3.2×10^{-3} (double), calculated by Student's t test. Box plots of γH2AX foci at the indicated time points (0, 0.3, and 6 h) are shown in Figure S5H.

comparison with *wild-type* cells (Biehs et al., 2017; Delacote et al., 2002; Gupta et al., 2018; Schipler and Iliakis, 2013; Zhang et al., 2011).

MRE11 Nuclease and UBC13-Dependent Ubiquitin Signaling Are Dispensable for NHEJ but Required for Efficient Repair of IR-Induced DSBs

Similar to *wild-type* cells, at 2 h after 4-OHT removal, the number of γH2AX foci per cell had declined to near background levels in UBC13-depleted (Figure S5B), BRCA1-depleted (Figure S5C), and MRE11 nuclease-deficient cells (Figures 5A and S5A). Thus, UBC13, BRCA1, and the nuclease activity of MRE11 are all dispensable for NHEJ. In contrast to *AsiSI*-mediated DSBs, IR-induced foci require a longer time (6 h) to drop back to background levels in *wild-type* cells (Figure 5B). The repair was NHEJ dependent as seen by the persistence of foci in $LIG4^{-/-}$ cells (Figure 5B). Interestingly, UBC13-depleted and $MRE11^{-/H129N}$ cells also showed the persistence of foci, approximately 54% and 69% of that in $LIG4^{-/-}$ mutant cells, respectively, at 6 h after IR exposure (Figures 5B and S5D). These values are probably an under-estimation of the actual contributions of UBC13 and MRE11 to the NHEJ of IR-induced DSBs since there were some residual UBC13 and MRE11 proteins left in their depleted cells. $LIG4^{-/-}/MRE11^{-/H129N}$ mutant cells (Figure S5E) did not show an increase in γH2AX foci compared with $LIG4^{-/-}$ mutant cells (Figures 5B and S5D). Thus, MRE11 nuclease activity collaborates with NHEJ-dependent repair, most likely by removing blocking adducts prior to NHEJ of clean DSBs. We conclude that MRE11 and UBC13 play a dominant role in the removal of blocking adducts from DSB ends preceding canonical NHEJ.

Although a previous study using shRNA to knockdown MRE11 reported nearly normal repair of IR-induced DSBs in MRE11-depleted cells (Biehs et al., 2017), we found a very severe defect in IR-induced DSB repair in MRE11 nuclease-deficient TK6 cells (Figures 5B and S5D). We thus tested the effect of MRE11 depletion on the repair of IR-induced DSBs in another cell line: HCT116 cells. To achieve a sufficient depletion of MRE11, we inserted auxin-induced-degron (AID) tag sequences into the endogenous *MRE11* allelic genes, generating $MRE11^{AID/AID}$ HCT116 cells (Figures S6A and S6B). When we depleted MRE11 using shRNA alone in HCT116 cells (Figure S6C), the depletion had very little effect on the repair of IR-induced DSBs during the G_1 phase (Figures 5C and S6D), as shown previously (Biehs et al., 2017). In marked contrast, cells simultaneously treated with auxin and shRNA showed delayed repair kinetics very similar to that of HCT116 cells treated with an inhibitor of DNA-PKcs to inhibit NHEJ (Figures 5C and S6D). The present results indicate that shRNA-mediated depletion of MRE11 might not be sufficient to identify the critical role of MRE11 in DSB repair. This observation of HCT116 cells is reminiscent of previous data indicating that a mere ~1% of the endogenous MRE11 protein is sufficient to effectively prevent the prominent phenotype, an accumulation of spontaneously arising mitotic chromosome breaks in TK6 cells (Hoa et al., 2015). We conclude that MRE11 is required for the removal of blocking adducts from IR-induced DSBs for subsequent NHEJ.

RNF8, RNF168, and BRCA1 Contribute to Cellular Tolerance to IR

Although BRCA1-depleted cells and $DNA\text{-}PKcs^{-/-}$ cells showed the same prominent delays in the repair of etoposide-induced DSBs in the G_1 phase (Figure 2C), BRCA1's contribution to the repair of IR-induced DSBs was less prominent than that of LIG4 (Figures 5B and S5D). We hypothesized that another enzyme(s) substituted for lack of BRCA1 and chose to analyze $BRCA1^{AID/AID}/RNF168^{-/-}$ TK6 cells because BRCA1 and RNF168 are compensatory in HDR (Zong et al., 2019). Like BRCA1-depleted cells ($BRCA1^{AID/AID}$ cells treated with auxin), $BRCA1^{AID/AID}/RNF168^{-/-}$ cells without auxin treatment showed the delayed repair of IR-induced DSBs in the G_1 phase (Figures 5D and S5F). The addition of auxin to deplete BRCA1 in the $BRCA1^{AID/AID}/RNF168^{-/-}$ cells caused a greater delay in the repair of IR-induced DSBs than the BRCA1-depleted $BRCA1^{AID/AID}$ cells (Figures 5D and S5F). We also examined the contribution of RNF8, another ubiquitin E3 ligase involved in DSB repair, to the repair of IR-induced DSBs in G_1-phase cells. We observed the delayed DSB repair in $RNF8^{-/-}$ cells (Figures 5E and S5H). The depletion of BRCA1 in $RNF8^{-/-}$ cells (shBRCA1/$RNF8^{-/-}$) caused a further delay in the repair of IR-induced DSBs, indicating a compensatory function of BRCA1 and RNF8 in the repair of IR-induced DSBs. Taken together, the data support the idea that removal of blocking adducts from IR-induced DSBs involves more complex ubiquitin signaling than that from etoposide-induced DSBs. RNF8 and RNF168 may mask the important role played by BRCA1 in the repair of IR-induced DSBs in the G_1 phase.

A Collaboration of ARTEMIS, EXD2, and EXO1 with MRE11 in the Repair of IR-Induced DSBs

We explored the role played by enzymes that are implicated in the processing of IR-induced DSBs in TK6 cells. We analyzed DNA polymerases β and θ, both of which have 5′ -deoxyribose phosphate (dRP) lyase activity (Prasad et al., 2009), TDP1, TDP2, PARP1, and XRCC1, the last two playing a key role in micro-homology-mediated end joining (MMEJ) (Figures S7A–S7D) (Saha et al., 2018) (Sfeir and Symington, 2015). TK6 cells deficient in these proteins were all tolerant to IR (Figure S7E). We also analyzed nucle-ases that process DSB ends during the G_1 phase, including ARTEMIS, EXD2, and EXO1 (Figures S7F–S7H) (Biehs et al., 2017). TK6 cells null-deficient in any of these three nucleases were all sensitive to IR (Figure S7E), but the phenotypes were milder than those of LIG4-deficient and MRE11 nuclease-deficient cells (Figures 5B and S5D). ARTEMIS has an overhang endonucleolytic processing activity (Ma et al., 2002; Pannunzio et al., 2018) and might remove blocking adducts attached to overhang sequences at DSBs. Neither EXD2 nor EXO1 may be able to remove blocking adducts from IR-induced DSBs. It is more likely that these two nucleases generate ligatable blunt-end and cohesive-end breaks (Pannunzio et al., 2018). In summary, these data indicate MRE11 nuclease plays a dominant role in the removal of blocking adducts to generate clean ends and ARTEMIS, EXD2, and EXO1 may subsequently process the clean DSBs for direct ligation by NHEJ.

DISCUSSION

We herein demonstrate that UBC13-mediated ubiquitin signaling plays a pivotal role in the removal of 5′ TOP2 adducts preceding NHEJ (Figures 1, 2, 3, and 4). This signaling is carried out most likely by RAP80 and BRCA1 and activates the MRE11 nuclease to remove 5′ TOP2 adducts. We also show that UBC13-mediated ubiquitin signaling and MRE11 are dispensable for rejoining of the AsiSI RE-induced DSBs (Figures 5A and S5A) but required for most NHEJ-dependent repair events in IR-irradiated G_1 cells (Figures 5B, 5C, S5D, and S6D). This finding indicates the crucial role played by both UBC13-mediated ubiquitin signaling and MRE11 in removing IR-induced blocking adducts in addition to TOP2 adducts from DSB ends. NHEJ re-pairs approximately 80% of the IR-induced DSBs even in the S/G_2 phases (Beucher et al., 2009) (Shibata et al., 2014) and plays a more important role in repairing etoposide-induced DSBs than does HDR (Maede et al., 2014). Moreover, the repair time of dirty DSBs induced by etoposide (Figures 1B, 2A, and 2C) and IR (Figures 5B–5E) was several times longer than that of RE-induced clean DSBs (Figure 5A). Considering these data, the current study sheds light on the removal of blocking adducts from dirty DSBs as the key rate-limiting step in the repair of DSBs generated by radiotherapy and a chemotherapy via etoposide during all phases of the cell cycle.

We have shown that MRE11 plays a dominant role in the removal of blocking adducts prior to NHEJ of clean DSBs in cells. Our results are supported by several biochemical studies that showed that non-co-valent DNA-bound KU70/80 proteins stimulate the endonuclease activity of MRE11, leading to the removal of adducts from both 3′ and 5′ termini at DSBs (Deshpande et al., 2016) (Deshpande et al., 2018) (Anand et al., 2019) (reviewed in Paull, 2018). Thus, MRE11-dependent elimination of various

chemical adducts attached to DSB ends may be a common mechanism for generating ligatable clean ends prior to direct ligation by canonical NHEJ. We also examined the contributions of other nucleases to the processing of dirty DSBs in the G_1 phase. ARTEMIS, EXD2, EXO1, and MRE11 contribute to approximately 36%, 39%, 45%, and 69%, respectively, of the NHEJ events during 6-h repair time post-IR in the G_1 phase (Figure 5B). Although exonucleases EXD2 or EXO1 may not be capable of removing various blocking adducts from DSB ends, the loss of ARTEMIS increases sensitivity to camptothecin, a TOP1 poison, but not etoposide (Maede et al., 2014), suggesting that ARTEMIS removes various 3' blocking adducts including TOP1 adducts from DSBs. ARTEMIS, EXD2, and EXO1 might generate blunt-end and cohesive-end breaks, which can be ligated by LIG4 after the removal of blocking adducts from DSB ends by MRE11. This notion is supported by the previous findings that DSB resection is executed by these nucleases in G_1 phase (Biehs et al., 2017). Identifying the roles played by ARTEMIS, EXD2, and EXO1 in the repair of IR-induced DSBs is an important area of study for the future. In contrast with the four nucleases, DNA polymerases β and θ, both of which have 5'-dRP lyase activity, TDP1, and TDP2 contribute only a little to the repair of IR-induced DSBs (Figure S7E). PARP1 and XRCC1, which play a key role in microhomology-mediated end joining (MMEJ) (Sfeir and Symington, 2015) are dispensable for the repair of IR-induced DSBs (Figure S7E), as previously reported (Simsek et al., 2011). In conclusion, ARTEMIS, EXD2, EXO1, and MRE11 all contribute to the repair of IR-induced DSBs in preparation for subsequent NHEJ. Given the dominant role played by MRE11, ARTEMIS, EXD2, and EXO1 may collaborate with MRE11 in the repair of IR-induced DSBs.

To protect genomic DNA from excess degradation, nuclease activity is strictly regulated (Symington, 2016). The mechanisms underlying MRE11 nuclease activity in the S/G_2 phases have been thoroughly studied, but it is unclear how MRE11 nuclease is regulated in the removal of chemical adducts from DSB ends during the G_1 phase. MRE11 nuclease activity is regulated by phosphorylation during DSB resection in the S/G_2 phases (Costanzo et al., 2001) (Falck et al., 2012) (Kijas et al., 2015). DSB resection is also promoted by UBC13-dependent ubiquitination of histones at DSB sites (reviewed in Uckelmann and Sixma, 2017), although the usage of the lysine residues on the ubiquitin is unclear. In the present study, we show that UBC13-mediated ubiquitination signaling is activated not only during the S/G_2 phases but also during the G_1 phase (Figure 1). Activation of ubiquitin signaling in the G_1 phase is required for the physical interaction between BRCA1 and MRE11 (Figure 4B), similar to S/G_2 phases (Zhao et al., 2007). The resulting BRCA1-MRE11 complex that forms at the DSB site is essential for the removal of etoposide-induced 5' TOP2 adducts. In addition to ubiquitin signaling-dependent BRCA1-MRE11 complex formation, CtIP, a regulatory factor of DSB end resection, also plays a critical role in the removal of blocking adducts. Biochemical studies demonstrated that phosphorylated CtIP stimulates MRE11 nuclease activity for the removal of blocking adducts (Anand et al., 2019, 2016; Quennet et al., 2011). CDK-dependent phosphorylation in CtIP is required for the removal of 5' TOP2 adducts by promoting the interaction between CtIP and BRCA1 (Aparicio et al., 2016; Nakamura et al., 2010). The phosphorylated CtIP is recognized by NBS1, which regulates the nuclease activity of MRE11-RAD50 complex (Anand et al., 2019; Deshpande et al., 2016). It is possible that phosphorylated CtIP regulates MRE11 nuclease activity by facilitating complex formation among BRCA1-MRN-CtIP at etoposide-induced DSB sites in G_1 phase. BRCA1 also promotes the removal of IR-induced chemical adducts by MRE11 prior to direct ligation of these processed DSBs by NHEJ. UBC13-mediated ubiquitination seems to activate complex signaling pathways involving multiple proteins, including BRCA1, RNF8, and RNF168 (Figures 5D and 5E), and contribute to the repair of IR-induced DSBs in the G_1 phase. In sum, UBC13-mediated ubiquitin signaling activates MRE11-dependent DSB end-processing. Future biochemical studies are needed to clarify how BRCA1 stimulates the endonuclease activity of MRE11.

We propose a model in which dirty DSBs, induced by etoposide and IR, are repaired during the G_1 phase. DSBs are rapidly recognized by the KU70/80 complex (step 2, Figures 6A and 6B). It remains unclear whether the KU70/80 complex interacts with DSB ends bearing intact TOP2 or interacts after TOP2 adducts are degraded by proteasome (Isik et al., 2003; Lee et al., 2018). TDP2 removes TOP2 adducts after its degradation by the proteasome (Lee et al., 2018). UBC13 catalyzes ubiquitination of histones at DSB sites in collaboration with ubiquitin E3 ligase(s), such as RNF8 and RNF168 (step 3, Figure 6B). The clean DSB ends induced by RE are quickly rejoined by NHEJ (step 3, Figure 6A). This ubiquitination (step 3, Figure 6B) facilitates the recruitment of multiple proteins such as BRCA1 and RAP80 onto the dirty DSB ends (step 4, Figure 6B). The recruited BRCA1 forms a stable complex with MRE11, with the resulting complex perhaps stimulating the endonuclease activity of MRE11 (step 5, Figure 6B).
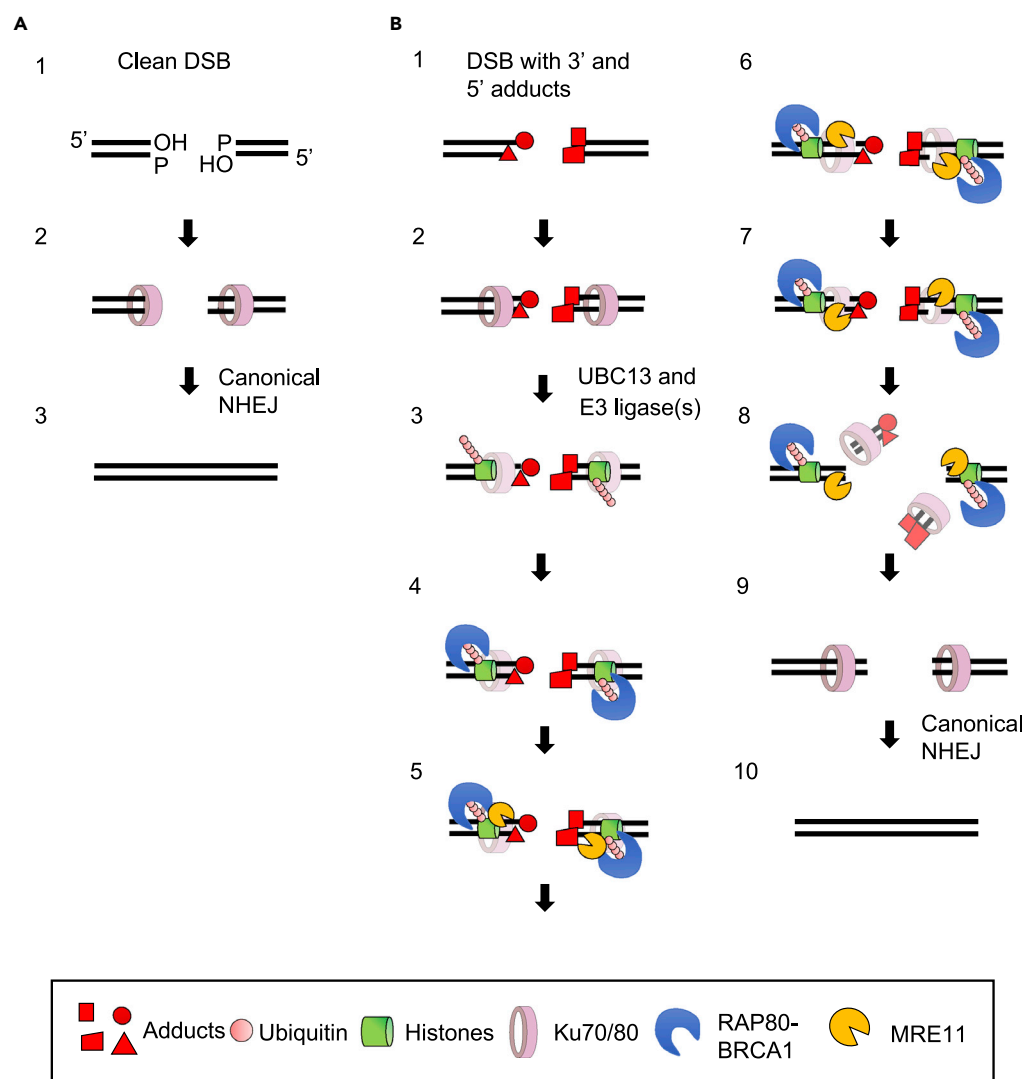
Figure 6. Proposed Model for Ten-Step Elimination of the Adducts Attached to DSB Ends

(A) Restriction enzyme generates "clean" DSBs with 3'- hydroxyl groups and 5'-phosphate ends (step 1). The DSB ends are rapidly recognized by the KU70/80 complex (step 2) and rejoined by canonical NHEJ (step 3).

(B) Ionizing radiation generates "dirty" DSBs associated with 3' and 5' adducts (step 1). The DSB ends are rapidly recognized by the KU70/80 complex (step 2). UBC13 promotes K63 ubiquitination at DSB sites (step 3), where this ubiquitination is recognized by the BRCA1-RAP80 complex (step 4). UBC13 and RAP80 are required for stable complex formation between BRCA1 and MRE11 at DSB sites (step 5). Endonucleolytic cleavage by MRE11 releases 5' and -3' adducts from the DSB ends (steps 6–8). The resulting clean DSB ends are again recognized by the KU70/80 complex (step 9), then ligated by canonical NHEJ (step 10).

It remains unclear how RNF168 promotes the repair of IR-induced DSBs. Non-covalent DNA-bound KU70/80 proteins also stimulate MRE11 endonuclease activity, as previously suggested (Deshpande et al., 2018) (Reginato et al., 2017). This stimulated MRE11 endonuclease engages in sequential endonucleolytic processing of both 5' and 3' termini and may completely remove both blocking adducts and KU70/80 proteins from the DSBs (steps 6 and 7, Figure 6B) (Deshpande et al., 2018) (reviewed in Paull, 2018). The resulting clean DSB ends are bound by KU70/80 proteins (step 9, Figure 6B), leading to rejoining of the DSBs by canonical NHEJ (step 10, Figure 6B). The mechanism by which a variety of chemicals adducts at IR-induced DSBs is likely to be much more complicated than that by which 5' TOP2 adducts are removed, with multiple mechanisms in play, depending on the structure of the dirty

DSB ends. Future study will shed light on the multiple mechanisms underlying the removal of a variety of chemical adducts prior to NHEJ.

Limitations of the Study

In this study, we identified the involvement of the UBC13-mediated ubiquitination pathway in the removal of blocking adducts generated not only by etoposide but also by ionizing radiation. Mechanistically, UBC13-mediated ubiquitination signaling strongly promotes the interaction between BRCA1 and MRE11, thereby stimulating nuclease activity of MRE11 for the removal of blocking adducts from DSB sites. The current study has not clearly demonstrated the molecular targets ubiquitinated by UBC13 at the DSB sites. This topic should be investigated in future work.

METHODS

All methods can be found in the accompanying Transparent Methods supplemental file.

SUPPLEMENTAL INFORMATION

Supplemental Information can be found online at https://doi.org/10.1016/j.isci.2020.101027.

AUTHOR CONTRIBUTIONS

This study was conceived by H.S. as well as S.T. Experiments and data analysis were performed by R.A., H.T.T., L.K.S., M.T., K.H., S.Y., A.S., M.T.K., S.N., and H.S. The paper was written by S.T. and H.S.

DECLARATION OF INTERESTS

The authors declare no competing interests.

REFERENCES

Alt, F.W., Zhang, Y., Meng, F.-L., Guo, C., and Schwer, B. (2013). Mechanisms of programmed DNA lesions and genomic instability in the immune system. Cell *152*, 417–429.

Anand, R., Jasrotia, A., Bundschuh, D., Howard, S.M., Ranjha, L., Stucki, M., and Cejka, P. (2019). NBS1 promotes the endonuclease activity of the MRE11-RAD50 complex by sensing CtIP phosphorylation. EMBO J. *38*, e101005.

Anand, R., Ranjha, L., Cannavo, E., and Cejka, P. (2016). Phosphorylated CtIP functions as a Co-factor of the MRE11-RAD50-NBS1 endonuclease in DNA end resection. Mol. Cell *64*, 940–950.

Aparicio, T., Baer, R., Gottesman, M., and Gautier, J. (2016). MRN, CtIP, and BRCA1 mediate repair of topoisomerase II-DNA adducts. J. Cell Biol. *212*, 399–408.

Asaithamby, A., Hu, B., and Chen, D.J. (2011). Unrepaired clustered DNA lesions induce chromosome breakage in human cells. Proc. Natl. Acad. Sci. U S A *108*, 8293–8298.

Averbeck, N.B., Ringel, O., Herrlitz, M., Jakob, B., Durante, M., and Taucher-Scholz, G. (2014). DNA end resection is needed for the repair of complex lesions in G1-phase human cells. Cell Cycle *13*, 2509–2516.

Aymard, F., Bugler, B., Schmidt, C.K., Guillou, E., Caron, P., Briois, S., Iacovoni, J.S., Daburon, V., Miller, K.M., Jackson, S.P., and Legube, G. (2014). Transcriptionally active chromatin recruits homologous recombination at DNA double-strand breaks. Nat. Struct. Mol. Biol. *21*, 366–374.

Bétermier, M., Bertrand, P., and Lopez, B.S. (2014). Is non-homologous end-joining really an inherently error-prone process? PLoS Genet. *10*, e1004086.

Beucher, A., Birraux, J., Tchouandong, L., Barton, O., Shibata, A., Conrad, S., Goodarzi, A.A., Krempler, A., Jeggo, P.A., and Löbrich, M. (2009). ATM and Artemis promote homologous recombination of radiation-induced DNA

double-strand breaks in G2. EMBO J. *28*, 3413–3427.

Biehs, R., Steinlage, M., Barton, O., Juhász, S., Künzel, J., Spies, J., Shibata, A., Jeggo, P.A., and Löbrich, M. (2017). DNA double-strand break resection occurs during non-homologous end joining in G1 but is distinct from resection during homologous recombination. Mol. Cell *65*, 671–684.e5.

Bohgaki, T., Bohgaki, M., Cardoso, R., Panier, S., Zeegers, D., Li, L., Stewart, G.S., Sanchez, O., Hande, M.P., Durocher, D., et al. (2011). Genomic instability, defective spermatogenesis, immunodeficiency, and cancer in a mouse model of the RIDDLE syndrome. PLoS Genet. *7*, e1001381.

Cannavo, E., and Cejka, P. (2014). Sae2 promotes dsDNA endonuclease activity within Mre11-Rad50-Xrs2 to resect DNA breaks. Nature *514*, 122–125.

Caron, P., Choudjaye, J., Clouaire, T., Bugler, B., Daburon, V., Aguirrebengoa, M., Mangeat, T., Iacovoni, J.S., Álvarez-Quilón, A., Cortés-Ledesma, F., and Legube, G. (2015). Non-redundant functions of ATM and DNA-PKcs in response to DNA double-strand breaks. Cell Rep. *13*, 1598–1609.

Chang, H.H.Y., Pannunzio, N.R., Adachi, N., and Lieber, M.R. (2017). Non-homologous DNA end joining and alternative pathways to double-strand break repair. Nat. Rev. Mol. Cell Biol. *18*, 495–506.

Chappell, C., Hanakahi, L.A., Karimi-Busheri, F., Weinfeld, M., and West, S.C. (2002). Involvement of human polynucleotide kinase in double-strand break repair by non-homologous end joining. EMBO J. *21*, 2827–2832.

Chen, L., Nievera, C.J., Lee, A.Y.-L., and Wu, X. (2008). Cell cycle-dependent complex formation of BRCA1.CtIP.MRN is important for DNA double-strand break repair. J. Biol. Chem. *283*, 7713–7720.

Costanzo, V., Robertson, K., Bibikova, M., Kim, E., Grieco, D., Gottesman, M., Carroll, D., and Gautier, J. (2001). Mre11 protein complex prevents double-strand break accumulation during chromosomal DNA replication. Mol. Cell *8*, 137–147.

Cowell, I.G., and Austin, C.A. (2012). Mechanism of generation of therapy related leukemia in response to anti-topoisomerase II agents. Int. J. Environ. Res. Public Health *9*, 2075–2091.

Davis, A.J., and Chen, D.J. (2014). Complex DSBs: a need for resection. Cell Cycle *13*, 3796–3797.

Delacote, F., Han, M., Stamato, T.D., Jasin, M., and Lopez, B.S. (2002). An xrcc4 defect or Wortmannin stimulates homologous recombination specifically induced by double-strand breaks in mammalian cells. Nucleic Acids Res. *30*, 3454–3463.

Deshpande, R.A., Lee, J.-H., Arora, S., and Paull, T.T. (2016). Nbs1 converts the human Mre11/Rad50 nuclease complex into an endo/exonuclease machine specific for protein-DNA adducts. Mol. Cell *64*, 593–606.

Deshpande, R.A., Myler, L.R., Soniat, M.M., Makharashvili, N., Lee, L., Lees-Miller, S.P., Finkelstein, I.J., and Paull, T.T. (2018). DNA-PKcs promotes DNA end processing. bioRxiv *64*, 395731.

Dinkelmann, M., Spehalski, E., Stoneham, T., Buis, J., Wu, Y., Sekiguchi, J.M., and Ferguson, D.O. (2009). Multiple functions of MRN in end-joining pathways during isotype class switching. Nat. Struct. Mol. Biol. *16*, 808–813.

Doil, C., Mailand, N., Bekker-Jensen, S., Menard, P., Larsen, D.H., Pepperkok, R., Ellenberg, J., Panier, S., Durocher, D., Bartek, J., et al. (2009). RNF168 binds and amplifies ubiquitin conjugates on damaged chromosomes to allow accumulation of repair proteins. Cell *136*, 435–446.

Dong, Z., Zhong, Q., and Chen, P.L. (1999). The Nijmegen breakage syndrome protein is essential for Mre11 phosphorylation upon DNA damage. J. Biol. Chem. *274*, 19513–19516.

Dynan, W.S., and Yoo, S. (1998). Interaction of Ku protein and DNA-dependent protein kinase catalytic subunit with nucleic acids. Nucleic Acids Res. *26*, 1551–1559.

Falck, J., Forment, J.V., Coates, J., Mistrik, M., Lukas, J., Bartek, J., and Jackson, S.P. (2012). CDK targeting of NBS1 promotes DNA-end resection, replication restart and homologous recombination. EMBO Rep. *13*, 561–568.

Garcia, V., Phelps, S.E.L., Gray, S., and Neale, M.J. (2011). Bidirectional resection of DNA double-strand breaks by Mre11 and Exo1. Nature *479*, 241–244.

Greenberg, R.A., Sobhian, B., Pathania, S., Cantor, S.B., Nakatani, Y., and Livingston, D.M. (2006). Multifactorial contributions to an acute DNA damage response by BRCA1/BARD1-containing complexes. Genes Dev. *20*, 34–46.

Gupta, R., Somyajit, K., Narita, T., Maskey, E., Stanlie, A., Kremer, M., Typas, D., Lammers, M., Mailand, N., Nussenzweig, A., et al. (2018). DNA repair network analysis reveals shieldin as a key regulator of NHEJ and PARP inhibitor sensitivity. Cell *173*, 972–988.e23.

Hartsuiker, E., Neale, M.J., and Carr, A.M. (2009). Distinct requirements for the Rad32(Mre11) nuclease and Ctp1(CtIP) in the removal of covalently bound topoisomerase I and II from DNA. Mol. Cell *33*, 117–123.

Hoa, N.N., Akagawa, R., Yamasaki, T., Hirota, K., Sasa, K., Natsume, T., Kobayashi, J., Sakuma, T., Yamamoto, T., Komatsu, K., et al. (2015). Relative contribution of four nucleases, CtIP, Dna2, Exo1 and Mre11, to the initial step of DNA double-strand break repair by homologous recombination in both the chicken DT40 and human TK6 cell lines. Genes Cells *20*, 1059–1076.

Hoa, N.N., Shimizu, T., Zhou, Z.W., Wang, Z.-Q., Deshpande, R.A., Paull, T.T., Akter, S., Tsuda, M., Furuta, R., Tsutsui, K., et al. (2016). Mre11 is essential for the removal of lethal topoisomerase 2 covalent cleavage complexes. Mol. Cell *64*, 580–592.

Hu, Y., Scully, R., Sobhian, B., Xie, A., Shestakova, E., and Livingston, D.M. (2011). RAP80-directed tuning of BRCA1 homologous recombination function at ionizing radiation-induced nuclear foci. Genes Dev. *25*, 685–700.

Huen, M.S.Y., Grant, R., Manke, I., Minn, K., Yu, X., Yaffe, M.B., and Chen, J. (2008). The E3 ubiquitin ligase RNF8 transduces the DNA damage signal via an ubiquitin-dependent signaling pathway. Cell *13190*, 901–914.

Iacovoni, J.S., Caron, P., Lassadi, I., Nicolas, E., Massip, L., Trouche, D., and Legube, G. (2010). High-resolution profiling of gammaH2AX around DNA double strand breaks in the mammalian genome. EMBO J. *29*, 1446–1457.

Isik, S., Sano, K., Tsutsui, K., Seki, M., Enomoto, T., Saitoh, H., and Tsutsui, K. (2003). The SUMO pathway is required for selective degradation of DNA topoisomerase IIβ induced by a catalytic inhibitor ICRF-193(1). FEBS Lett. *546*, 374–378.

Jachimowicz, R.D., Beleggia, F., Isensee, J., Velpula, B.B., Goergens, J., Bustos, M.A., Doll, M.A., Shenoy, A., Checa-Rodriguez, C., Wiederstein, J.L., et al. (2019). UBQLN4 represses homologous recombination and is overexpressed in aggressive tumors. Cell *176*, 505–519.e22.

Jasin, M., and Haber, J.E. (2016). The democratization of gene editing: insights from site-specific cleavage and double-strand break repair. DNA Repair (Amst.) *44*, 6–16.

Jeggo, P.A., Geuting, V., and Löbrich, M. (2011). The role of homologous recombination in radiation-induced double-strand break repair. Radiother. Oncol. *101*, 7–12.

Kijas, A.W., Lim, Y.C., Bolderson, E., Cerosaletti, K., Gatei, M., Jakob, B., Tobias, F., Taucher-Scholz, G., Gueven, N., Oakley, G., et al. (2015). ATM-dependent phosphorylation of MRE11 controls extent of resection during homology directed repair by signalling through Exonuclease 1. Nucleic Acids Res. *43*, 8352–8367.

Kim, H., Chen, J., and Yu, X. (2007). Ubiquitin-binding protein RAP80 mediates BRCA1-dependent DNA damage response. Science *316*, 1202–1205.

Kolas, N.K., Chapman, J.R., Nakada, S., Ylanko, J., Chahwan, R., Sweeney, F.D., Panier, S., Mendez, M., Wildenhain, J., Thomson, T.M., et al. (2007). Orchestration of the DNA-damage response by the RNF8 ubiquitin ligase. Science *318*, 1637–1640.

Ledesma, F.C., El Khamisy, S.F., Zuma, M.C., Osborn, K., and Caldecott, K.W. (2009). A human 5′-tyrosyl DNA phosphodiesterase that repairs topoisomerase-mediated DNA damage. Nature *461*, 674–678.

Lee, K., Swan, R., Sondka, Z., Padget, K., Cowell, I., and Austin, C. (2018). Effect of TDP2 on the level of TOP2-DNA complexes and SUMOylated TOP2-DNA complexes. Int. J. Mol. Sci. *19*, 2056.

Lisby, M., Barlow, J.H., Burgess, R.C., and Rothstein, R. (2004). Choreography of the DNA damage response. Cell *118*, 699–713.

Ma, Y., Pannicke, U., Schwarz, K., and Lieber, M.R. (2002). Hairpin opening and overhang processing by an artemis/DNA-dependent protein kinase complex in nonhomologous end joining and V(D) J recombination. Cell 108, 781–794.

Maede, Y., Shimizu, H., Fukushima, T., Kogame, T., Nakamura, T., Miki, T., Takeda, S., Pommier, Y., and Murai, J. (2014). Differential and common DNA repair pathways for topoisomerase I- and II-targeted drugs in a genetic DT40 repair cell screen panel. Mol. Cancer Ther. 13, 214–220.

Mattiroli, F., Vissers, J.H.A., van Dijk, W.J., Ikpa, P., Citterio, E., Vermeulen, W., Marteijn, J.A., and Sixma, T.K. (2012). RNF168 ubiquitinates K13-15 on H2A/H2AX to drive DNA damage signaling. Cell 150, 1182–1195.

Mimitou, E.P., and Symington, L.S. (2008). Sae2, Exo1 and Sgs1 collaborate in DNA double-strand break processing. Nature 455, 770–U3.

Mladenov, E., Saha, J., and Iliakis, G. (2018). Processing-Challenges Generated by Clusters of DNA Double-Strand Breaks Underpin Increased Effectiveness of High-LET Radiation and Chromothripsis (Springer), pp. 149–168.

Moreau, S., Ferguson, J.R., and Symington, L.S. (1999). The nuclease activity of Mre11 is required for meiosis but not for mating type switching, end joining, or telomere maintenance. Mol. Cell. Biol. 19, 556–566.

Moynahan, M.E., and Jasin, M. (2010). Mitotic homologous recombination maintains genomic stability and suppresses tumorigenesis. Nat. Rev. Mol. Cell Biol. 11, 196–207.

Nakada, S. (2016). Opposing roles of RNF8/RNF168 and deubiquitinating enzymes in ubiquitination-dependent DNA double-strand break response signaling and DNA-repair pathway choice. J. Radiat. Res. 57, i33–i40.

Nakamura, K., Kogame, T., Oshiumi, H., Shinohara, A., Sumitomo, Y., Agama, K., Pommier, Y., Tsutsui, K.M., Tsutsui, K., Hartsuiker, E., et al. (2010). Collaborative action of Brca1 and CtIP in elimination of covalent modifications from double-strand breaks to facilitate subsequent break repair. PLoS Genet. 6, e1000828.

Nickoloff, J.A., Jones, D., Lee, S.-H., Williamson, E.A., and Hromas, R. (2017). Drugging the cancers addicted to DNA repair. J. Natl. Cancer Inst. 109, 1–13.

Nitiss, J.L. (2009). DNA topoisomerase II and its growing repertoire of biological functions. Nat. Rev. Cancer 9, 327–337.

O'Driscoll, M., and Jeggo, P.A. (2006). The role of double-strand break repair — insights from human genetics. Nat. Rev. Genet. 7, 45.

Oh, J., and Symington, L.S. (2018). Role of the Mre11 complex in preserving genome integrity. Genes (Basel) 9, 589.

Pannunzio, N.R., Watanabe, G., and Lieber, M.R. (2018). Nonhomologous DNA end-joining for repair of DNA double-strand breaks. J. Biol. Chem. 293, 10512–10523.

Paull, T.T. (2018). 20 Years of Mre11 Biology: no end in sight. Mol. Cell 71, 419–427.

Polanowska, J., Martin, J.S., Garcia-Muse, T., Petalcorin, M.I.R., and Boulton, S.J. (2006). A conserved pathway to activate BRCA1-dependent ubiquitylation at DNA damage sites. EMBO J. 25, 2178–2188.

Pommier, Y., Sun, Y., Huang, S.Y.N., and Nitiss, J.L. (2016). Roles of eukaryotic topoisomerases in transcription, replication and genomic stability. Nat. Rev. Mol. Cell Biol. 17, 703–721.

Prasad, R., Longley, M.J., Sharief, F.S., Hou, E.W., Copeland, W.C., and Wilson, S.H. (2009). Human DNA polymerase possesses 5'-dRP lyase activity and functions in single-nucleotide base excision repair in vitro. Nucleic Acids Res. 37, 1868–1877.

Quennet, V., Beucher, A., Barton, O., Takeda, S., and Löbrich, M. (2011). CtIP and MRN promote non-homologous end-joining of etoposide-induced DNA double-strand breaks in G1. Nucleic Acids Res. 39, 2144–2152.

Reginato, G., Cannavo, E., and Cejka, P. (2017). Physiological protein blocks direct the Mre11-Rad50-Xrs2 and Sae2 nuclease complex to initiate DNA end resection. Genes Dev. 31, 2325–2330.

Robins, P., and Lindahl, T. (1996). DNA ligase IV from HeLa cell nuclei. J. Biol. Chem. 271, 24257–24261.

Roques, C., Coulombe, Y., Delannoy, M., Vignard, J., Grossi, S., Brodeur, I., Rodrigue, A., Gautier, J., Stasiak, A.Z., Stasiak, A., et al. (2009). MRE11–RAD50–NBS1 is a critical regulator of FANCD2 stability and function during DNA double-strand break repair. EMBO J. 28, 2400–2413.

Saha, L.K., Kim, S., Kang, H., Akter, S., Choi, K., Sakuma, T., Yamamoto, T., Sasanuma, H., Hirota, K., Nakamura, J., et al. (2018). Differential micronucleus frequency in isogenic human cells deficient in DNA repair pathways is a valuable indicator for evaluating genotoxic agents and their genotoxic mechanisms. Environ. Mol. Mutagen. 59, 529–538.

Sasanuma, H., Tsuda, M., Morimoto, S., Saha, L.K., Rahman, M.M., Kiyooka, Y., Fujiike, H., Cherniack, A.D., Itou, J., Callen Moreu, E., et al. (2018). BRCA1 ensures genome integrity by eliminating estrogen-induced pathological topoisomerase II-DNA complexes. Proc. Natl. Acad. Sci. U S A 115, E10642–E10651.

Sato, Y., Yoshikawa, A., Mimura, H., Yamashita, M., Yamagata, A., and Fukai, S. (2009). Structural basis for specific recognition of Lys 63-linked polyubiquitin chains by tandem UIMs of RAP80. EMBO J. 28, 2461–2468.

Schipler, A., and Iliakis, G. (2013). DNA double-strand-break complexity levels and their possible contributions to the probability for error-prone processing and repair pathway choice. Nucleic Acids Res. 41, 7589–7605.

Sfeir, A., and Symington, L.S. (2015). Microhomology-mediated end joining: a back-up survival mechanism or dedicated pathway? Trends Biochem. Sci. 40, 701–714.

Shi, W., Ma, Z., Willers, H., Akhtar, K., Scott, S.P., Zhang, J., Powell, S., and Zhang, J. (2008). Disassembly of MDC1 foci is controlled by

ubiquitin-proteasome-dependent degradation. J. Biol. Chem. 283, 31608–31616.

Shibata, A., Moiani, D., Arvai, A.S., Perry, J., Harding, S.M., Genois, M.M., Maity, R., van Rossum-Fikkert, S., Kertokalio, A., Romoli, F., et al. (2014). DNA double-strand break repair pathway choice is directed by distinct MRE11 nuclease activities. Mol. Cell 53, 7–18.

Shrivastav, M., De Haro, L.P., and Nickoloff, J.A. (2008). Regulation of DNA double-strand break repair pathway choice. Cell Res. 18, 134–147.

Simsek, D., Furda, A., Gao, Y., Artus, J., Brunet, E., Hadjiantonakis, A.-K., Van Houten, B., Shuman, S., McKinnon, P.J., and Jasin, M. (2011). Crucial role for DNA ligase III in mitochondria but not in Xrcc1-dependent repair. Nature 471, 245–248.

Sobhian, B., Shao, G., Lilli, D.R., Culhane, A.C., Moreau, L.A., Xia, B., Livingston, D.M., and Greenberg, R.A. (2007). RAP80 targets BRCA1 to specific ubiquitin structures at DNA damage sites. Science 316, 1198–1202.

Stewart, G.S., Panier, S., Townsend, K., Al-Hakim, A.K., Kolas, N.K., Miller, E.S., Nakada, S., Ylanko, J., Olivarius, S., Mendez, M., et al. (2009). The RIDDLE syndrome protein mediates a ubiquitin-dependent signaling cascade at sites of DNA damage. Cell 136, 420–434.

Symington, L.S. (2016). Mechanism and regulation of DNA end resection in eukaryotes. Crit. Rev. Biochem. Mol. Biol. 51, 195–212.

Uckelmann, M., and Sixma, T.K. (2017). Histone ubiquitination in the DNA damage response. DNA Repair (Amst.) 56, 92–101.

Wang, B., and Elledge, S.J. (2007). Ubc13/Rnf8 ubiquitin ligases control foci formation of the Rap80/Abraxas/Brca1/Brcc36 complex in response to DNA damage. Proc. Natl. Acad. Sci. U S A 104, 20759–20763.

Wang, B., Matsuoka, S., Ballif, B.A., Zhang, D., Smogorzewska, A., Gygi, S.P., and Elledge, S.J. (2007). Abraxas and RAP80 form a BRCA1 protein complex required for the DNA damage response. Science 316, 1194–1198.

Westmoreland, J.W., and Resnick, M.A. (2013). Coincident resection at both ends of random, γ-induced double-strand breaks requires MRX (MRN), Sae2 (Ctp1), and Mre11-nuclease. PLoS Genet. 9, e1003420.

Woodbine, L., Brunton, H., Goodarzi, A.A., Shibata, A., and Jeggo, P.A. (2011). Endogenously induced DNA double strand breaks arise in heterochromatic DNA regions and require ataxia telangiectasia mutated and Artemis for their repair. Nucleic Acids Res. 39, 6986–6997.

Woodbine, L., Gennery, A.R., and Jeggo, P.A. (2014). Reprint of "The clinical impact of deficiency in DNA non-homologous end-joining". DNA Repair (Amst.) 17, 9–20.

Yamamoto, M., Okamoto, T., Takeda, K., Sato, S., Sanjo, H., Uematsu, S., Saitoh, T., Yamamoto, N., Sakurai, H., Ishii, K.J., et al. (2006). Key function for the Ubc13 E2 ubiquitin-conjugating enzyme in

immune receptor signaling. Nat. Immunol. *7*, 962–970.

Yin, Z., Menendez, D., Resnick, M.A., French, J.E., Janardhan, K.S., and Jetten, A.M. (2012). RAP80 is critical in maintaining genomic stability and suppressing tumor development. Cancer Res. *72*, 5080–5090.

Zhang, S., Yajima, H., Huynh, H., Zheng, J., Callen, E., Chen, H.-T., Wong, N., Bunting, S., Lin, Y.-F.,

Li, M., et al. (2011). Congenital bone marrow failure in DNA-PKcs mutant mice associated with deficiencies in DNA repair. J. Cell Biol. *193*, 295–305.

Zhao, G.Y., Sonoda, E., Barber, L.J., Oka, H., Murakawa, Y., Yamada, K., Ikura, T., Wang, X., Kobayashi, M., Yamamoto, K., et al. (2007). A critical role for the ubiquitin-conjugating enzyme Ubc13 in initiating homologous recombination. Mol. Cell *25*, 663–675.

Zhu, Z., Chung, W.-H., Shim, E.Y., Lee, S.E., and Ira, G. (2008). Sgs1 helicase and two nucleases Dna2 and Exo1 resect DNA double-strand break ends. Cell *134*, 981–994.

Zong, D., Adam, S., Wang, Y., Sasanuma, H., Callén, E., Murga, M., Day, A., Kruhlak, M.J., Wong, N., Munro, M., et al. (2019). BRCA1 haploinsufficiency is masked by RNF168-mediated chromatin ubiquitylation. Mol. Cell *73*, 1267–1281.e7.

Supplemental Information

UBC13-Mediated Ubiquitin Signaling

Promotes Removal of Blocking Adducts

from DNA Double-Strand Breaks

Remi Akagawa, Hai Thanh Trinh, Liton Kumar Saha, Masataka Tsuda, Kouji Hirota, Shintaro Yamada, Atsushi Shibata, Masato T. Kanemaki, Shinichiro Nakada, Shunichi Takeda, and Hiroyuki Sasanuma

UBC13-mediated ubiquitin signaling promotes removal of blocking adducts from

DNA double-strand breaks

Remi Akagawa, Hai Thanh Trinh, Liton Kumar Saha, Masataka Tsuda, Kouji Hirota, Shintaro Yamada, Atsushi Shibata, Masato T. Kanemaki, Shinichiro Nakada, Shunichi Takeda[*], and Hiroyuki Sasanuma[*]

[*] Corresponding authors

SUPPLEMENTAL INFORMATION

TRANSPARENT METHODS

SUPPLEMENTAL FIGURES AND FIGURE LEGENDS

TRANSPARENT METHODS

Key resource table

Reagent or Resource	Source	Identifier
Antibodies		
Mouse monoclonal α-Multi Ubiquitin mAb (clone FK2)	MBL	Cat# D058-3
Rabbit polyclonal α-53BP1	Calbiochem	Cat# PC712-100UL
Mouse monoclonal α-γH2AX (clone JBW301)	Millipore	Cat# 05-636, RRID:AB_309864
Rabbit monoclonal α-γH2AX	Cell Signaling Technology	Cat# 9718, RRID:AB_2118009
Rabbit polyclonal α-CyclinA (clone C19)	Santa Cruz	Cat# sc-596, RRID:AB_631330
Rabbit polyclonal α-RAP80	Novus Biologicals	Cat# NBP1-87156
Rabbit polyclonal α-RAP80	Bethyl Laboratories	Cat# A300-763A
Mouse monoclonal α-BRCA1 (clone D9)	Santa Cruz	Cat# sc-6954, RRID:AB_626761
Rabbit polyclonal α-BRCA1	Abcam	Cat# ab9141 RRID:AB 307041
Mouse monoclonal α-TOP2β	(Tsutsui et al., 2001)	N/A

Mouse monoclonal α-MRE11 (clone 12D7)	Gene Tex	Cat# GTX70212, RRID:AB_372398
Mouse monoclonal α-LIG4 (clone D-8)	Santa Cruz	Cat# sc-271299
Mouse monoclonal α-PARP1 (clone H-250)	Santa Cruz	Cat# sc-7150
Rabbit polyclonal α-TDP1	Bethyl Laboratories	Cat# A301-618A
Rabbit polyclonal α-TDP2	Bethyl Laboratories	Cat# A302-737A
Mouse monoclonal α-β-actin	Sigma	Cat# A5411
Mouse monoclonal α-DNA-PKcs (clone 18-2)	Abcam	Cat# ab1832
Mouse monoclonal α-UBC13 (clone F-10)	Santa Cruz	Cat# sc-376470
Mouse monoclonal α-RNF8 (clone B-2)	Santa Cruz	Cat# sc-271462
α-BrdU	Becton, Dickinson and Company	Cat# 555627
Goat polyclonal α-mouse AlexaFluor 488	ThermoFisher	Cat# A-11029, RRID:AB_2534088
Goat polyclonal α-rabbit AlexaFluor 488	ThermoFisher	Cat# A-11034, RRID:AB_2576217

Goat polyclonal α-mouse AlexaFluor 594	ThermoFisher	Cat# A-11032, RRID: AB_2534091
Goat polyclonal α-rabbit AlexaFluor 594	ThermoFisher	Cat# A11037, RRID:AB_2534095
Goat polyclonal α-mouse HRP	ThermoFisher	Cat# 32430
Donkey polyclonal α-rabbit HRP	Santa Cruz	Cat# sc-2313, RRID:AB_641181
α-mouse Ig, FITC conjugate	SBA	Cat# 1031-02
Chemicals, Peptides, and Recombinant Proteins		
Charcoal/Dextran treated FBS	Hyclone Laboratories	Cat#SH30068.03
Albumin, Bovine, F-V, pH5.2	Nacalai Tesque	Cat# 01863-48
Skim Milk for immunoassay	Nacalai Tesque	Cat# 31149-75
Paraformaldehyde	Wako	Cat# 16320145
FuGENE HD Transfection Reagent	Promega	Cat# E2312
Doxycycline Hydrochloride	MP Biomedicals, Inc.	Cat# 195044
Fluoro-KEEPER Antifade Reagent	Nacalai Tesque	Cat# 12745-74
Etoposide	Trevigen	Cat# 4886-400-01
KU7441	Selleckchem.com	Cat# S2638
3'-Indoleacetic Acid	Nacalai Tesque	Cat# 19119-61
2.5 g/l-Tripsin/1 mmol/l-EDTA Solution	Nacalai Tesque	Cat# 35554-64
Propidium iodine (PI)	DOJINDO	Cat# P378
BrdU	Nacalai Tesque	Cat# 05650-66
Critical Commercial Assays		

GeneArt Seamless Cloning Enzyme Mix	ThermoFisher	Cat# A14606
Stbl3	ThermoFisher	Cat# C737303
X10-gold Ultracompetent cells	Ajilent	Cat# 200314
Experimental Models: Cell Lines		
Human: MCF7, *wild-type*	ATCC	Cat# HTB-22
Human: TK6 (TSCER2), *wild-type*	A gift from Dr. Masamitsu Honma (Honma et al., 2003)	N/A
Human: HCT116 WT, *wild-type*	A gift from Dr. Masato Kanemaki	N/A
Human: Lenti-X™ 293T	TAKARA	Cat# 632180
Experimental Models: Organisms/Strains		
The mutant genotypes of TK6, MCF7, and HCT116 are listed in Table S1	This work	
Oligonucleotides		
The primers are listed in Table S2	This work	
Recombinant DNA		
Plasmid: px330-U6-Chimeric_BB-CBh-hSpCas9	Addgene	Cat# 42230
Plasmid: *DT-ApA/MARKER^R*	CDB, RIKEN, Kobe	N/A
Plasmid: pSpCas9(BB)-2A-Puro(pX459)	(Ran et al., 2013)	Cat# 48139
Plasmid: lentiCRISPRv2-neo	Addgene	Addgene#98292
Plasmid: pLKO.1	(Hoa et al., 2016)	Cat#8453
Plasmid: pMD2.G	Addgene	Cat #12259
Plasmid: pMDLg/pRRE		Cat#8453

Plasmid: pRSV-Rev		Cat#12253
Plasmid: lentiCRISPRv2-*Asi*SI	A gift from Tanya Paull	N/A

Contact for reagent and resource sharing

Further information and requests for resources and reagents should be directed to and

will be fulfilled by the Lead Contact, Hiroyuki Sasanuma (hiroysasa@rg.med.kyoto-

u.ac.jp)

Experimental model and subject details

Mutant cells and primer sequences used in this paper are described in Tables S1 and S2,

respectively.

Method details

Cell culture

Human TK6 B cells were incubated in RPMI1640 medium (Cat# 3026456, Nacalai

Tesque, Japan) supplemented with horse serum (5%) (Gibco, US), penicillin (100

U/ml), streptomycin (100 μg/ml) (Nacalai, Japan), and sodium pyruvate (200 mg/ml)

(ThermoFisher, US). MCF-7 cells were maintained in Dulbecco's Modified Eagle

Medium (DMEM) (Cat# 0845964, Gibco, US) containing fetal bovine serum (10%)

(Gibco, US), penicillin (100 U/ml), and streptomycin (100 μg/ml) (Nacalai, Japan).

HCT116 cells were maintained in McCoy's 5A medium (Cat# SH30200.01, GE

Healthcare, US) containing fetal bovine serum (10%) (Gibco, US), penicillin (100

U/ml), streptomycin (100 µg/ml) (Nacalai, Japan), and L-Glutamine (Nacalai, Japan).

Lenti-X™ 293T cells (Cat# 632180, TAKARA, Japan) were maintained in DMEM

supplemented with fetal bovine serum (10%), penicillin (100 U/ml), streptomycin (100

µg/ml) (Nacalai, Japan), sodium pyruvate (200 mg/ml) and L-glutamine (Nacalai,

Japan). TK6, MCF-7, HCT116 and Lenti-X™ 293T cells were maintained at 37℃

under a humidified atmosphere and CO_2 (5%).

Designing gene-targeting constructs and transfection of them into TK6 cells

We designed gene-targeting constructs based on the manual provided by GeneArt

Seamless Cloning Enzyme Mix (ThermoFischer, US)(Hoa et al., 2016). Table S1 shows

the list of mutants and the antibiotic resistance markers (*MARKER^R*) used to generate

the mutants in this study. To generate gene-targeting constructs, we amplified left and

right arms (~1 kb each) from genomic DNA. The amplified arms were assembled with

the *DT-ApA/MARKER^R vector digested with ApaI* and the *AflII* using GeneArt Seamless

Cloning Enzyme Mix (ThermoFischer, US). Primer information about the left and right

arms (~1 kb each) is described in Table S2. To generate the left arm, we needed to add

the upstream and downstream sequences derived from the *ApaI* site *to the 5' and 3'*

ends, respectively, of the PCR-amplified left arm. For this purpose, we added "5'-

GCGAATTGGGTACCGGGCC" to 5' of the upstream primer and added "5'-

CTGGGCTCGAGGGGGGGCC" to 5' of the downstream primer. We added the

upstream and downstream sequences from the *AflII* site *to the 5' and 3' ends,*

respectively, of the right arm. We added "5'-TGGGAAGCTTGTCGACTTAA" to 5' of

the upstream primer of the PCR-amplified right arm and added "5'-

CACTAGTAGGCGCGCCTTAA" to 5' of the downstream primer of the PCR-amplified right arm. The *DT-ApA/MARKER^R* was provided by the Laboratory for Animal Resources and Genetic Engineering, Center for Developmental Biology, RIKEN Kobe (http://www.clst.riken.jp/arg/cassette.html).

The gRNAs were inserted into the *BbsI* site of pX330 vector (Cat# 42230, Addgene, US). The two resulting targeting vectors containing different antibiotic markers were transfected with pX330-gRNA into six million TK6 cells. The transfected pX330 expressed the Cas9-gRNA complex, which induced DSBs at the specific locus of the genomic DNA and thus facilitated HR between the genomic locus and the arms of the targeting vectors.

Generation of TK6 mutant cells

Schematic diagrams of *RAP80*, *RNF8, POLβ, POLQ, TDP1*, *PARP1, ARTEMIS*, *EXD2*, and *EXO1* target locations are depicted in Figures S2A, S3C, S7A-D and S7F-H. Generation of *BRCA1^{AID/AID}*, *BRCA1^{AID/AID}/RNF168^{-/-}*, *XRCC1^{-/-}*, and *MRE11^{-/H129N}* cells was as described previously (Hoa et al., 2016, 2015; Keka et al., 2015; Saha et al., 2018; Sasanuma et al., 2018)(Zong et al., 2019). To generate *TDP1^{-/-}/TDP2^{-/-}* and *LIG4^{-/-}/MRE11^{-/H129N}* mutant cells, we disrupted *TDP2* genes in *TDP1^{-/-}* cells and *LIG4* genes in *MRE11^{loxP/H129N}* cells (Figures S7C and S5E). PCR genotyping using the primers shown in Table S2 was performed as a primary screening. The gene-disruption events were confirmed by western blotting, reverse transcription-PCR (RT-PCR), or Southern blotting analysis. Disruption of *EXO1* alleles was confirmed by genomic Southern blotting using a ^{32}P-labeled probe, which was amplified by the following primer pair:

5'-CCATGCTAGTGAAAATTGAGAACAACTTTT and 5'-CTCCTTACTTTATACATCAGCATTACTGAA (Figure S7H). Genomic DNA was digested with *Hind*III for Southern blotting analysis.

CRISPR/Cas9-mediated genome-editing in human MCF-7 cells

The gRNA sequences are shown in Table S2. gRNAs were inserted into the *BbsI* site of pX459 (Cat# 48139, Addgene, US). pX459 expresses both a gRNA under the control of the U6 promoter and Cas9 driven by the chicken β-actin promoter. Schematic diagrams of the *DNA-PKcs* and *RAP80* target locations are presented in Figures S1G and S2A, respectively. pX459-gRNA was transfected into MCF-7 cells with FuGENE HD (Promega, US). Following transfection, cells were incubated with puromycin-containing medium for 48 h, after which we removed the puromycin and further incubated the cells (for approximately 2 weeks) to isolate the clones. Gene-disruption events were confirmed by western blotting.

CRISPR/Cas9-mediated genome-editing in human HCT116 cells

The C-terminus of endogenous *MRE11* was fused with mAID-GFP in HCT116 cells constitutively expressing OsTIR1 (Natsume et al., 2016). We inserted gRNA into pX330-U3-Chimeric_BB-CBh-hSpCas9 (Addgene #42230) to cut 31bp downstream of the stop codon (Figure S7A). We constructed two donor plasmids, each containing a knock-in cassette that encodes mAID-GFP with a neomycin or hygromycin resistance marker. The donors harbor homology arms (about 1 kb) at both ends of the knock-in cassette for integration by homology-directed repair. CRISPR and donor plasmids were co-transfected into HCT116 CMV-OsTIR1 cells. Cells were selected in the presence of

G418 (700 µg/mL) and HygroGold (100 µg/mL) following a publicly available protocol (Yesbolatova et al., 2019). Isolated clones were evaluated by genomic PCR to verify the bi-allelic integration, and the expression of the MRE11-mAID-GFP protein was confirmed by western blotting.

Cell-cycle analysis

Cells were labeled for 15 min with 50 µM BrdU. They were then harvested and fixed at 4°C overnight with 70% ethanol, and successively incubated as follows: (i) in 2N HCl, 0.5% Triton X-100 for 30 min at room temperature; (ii) in FITC-conjugated anti-BrdU antibody (Becton, Dickinson and Company, Franklin Lakes, NJ) for 30 min at room temperature; (iii) in FITC- conjugated anti - mouse antibody (Southern Biotech, Birmingham, AL) for 30 min at room temperature; (iv) in 5 µg/ml PI in PBS. Subsequent flow cytometric analysis was performed on an LSRFortessa (Becton, Dickinson and Company). Fluorescence data were displayed as dot plots using the Cell Quest software (Becton, Dickinson and Company).

Measurement of cellular sensitivity to DNA damaging agents

Cellular sensitivity of an asynchronous population of TK6 cells to etoposide and IR was measured by clonogenic cell-survival analysis. Cells were grown in the respective medium described above, containing methylcellulose, for 10 days. Cellular sensitivity of an asynchronous population of MCF-7 cells to etoposide was measured by clonogenic cell-survival analysis. Cells were grown in the respective medium described above for 10 days.

Measurement of TOP2 trapped on genomic DNA DSBs

The protocol for this assay was as described by Hoa *et al*. 2016. TOP2ccs that migrated into the CsCl gradient during ultra-centrifugation were detected by slot blot.

Lentivirus-mediated gene silencing and *Asi*SI expression

Lentiviral vectors were simultaneously transfected with virus-packaging plasmids (pMD2.G, pMDLg/pRRE, and pRSV-Rev) into LentiX-293T cells (Cat# 632180, Takara, Japan). Lentiviruses were harvested at 48 h post-transfection. MCF-7 cells were infected with the virus for 48 h. Puromycin was added to enrich the infected cells at 24 h after infection. For gene silencing, shRNA sequences targeting MRE11 (5'-CGACTGCGAGTGGACTATAGC), UBC13 (5'-CTAGGCTATATGCCATGAATA) and BRCA1 (5'-CCCTAAGTTTACTTCTCTAAA) were cloned into a pLKO.1 lentiviral vector (Table S2). Downregulation of MRE11, UBC13, and BRCA1 was confirmed by western blotting (Figures S1C, S2G, S5B, S5C, and S6C). To obtain TK6 cells stably expressing regulatable *Asi*SI RE coupled to an estrogen receptor (ER-*Asi*SI) in cells (Caron et al., 2015)(Aymard et al., 2014), the lentiviral lentiCRISPRv2 vector containing both ER-*Asi*SI and puromycin-resistance genes (a gift from Gaëlle Legube and Tanya Paull) was transfected into the LentiX-293T cells. The lentiviral particles were harvested at 48 h post transfection and were infected into the TK6 cells.

To express ER-*Asi*SI in *MRE11*$^{-/H129N}$ TK6 cells (Figure 5A), we treated *MRE11*$^{+/H129N}$ cells with 4-OHT (200 nM) for 24 h to inactivate the *wild-type MRE11* gene, generating *MRE11*$^{-/H129N}$ cells. After 4-OHT was washed out from the medium, lentiviral particles expressing ER-*Asi*SI were infected into the 4-OHT-treated *MRE11*$^{-/H129N}$ cells. After

incubating the infected cells for two days, we analyzed the ER-*Asi*SI-induced γH2AX foci by addition of 4-OHT into the medium.

Immuno-staining of γH2AX in TK6 cells

Cells were treated with etoposide (10 μM) for 30 minutes and IR, and subsequently washed twice with warm PBS and cultured in drug-free media. Cells were collected using a cytospin (ThermoFisher, US) and subjected to fixation by formaldehyde (4%) (Wako, Japan) in PBS, permeabilization by Tween-20 (0.1%) (23926-35, Nacalai Tesque) in PBS, and blocking by BSA (5%) (01683-48, Nacalai Tesque) in PBS. We used α-phospho (Ser139) -histone H2AX (anti-γH2AX) antibody (1/1000 dilution, JBW301, Millipore, US). To distinguish cells in the G_1 phase from other phases, we used a α-cyclinA antibody (1/100 dilution, G0811, Santa Cruz Biotechnology, US). The slides were mounted in Fluoro-KEEPER containing 4', 6-diamidino-2-phenylindole (DAPI) (12745-74, Nacalai Tesque, Japan).

Immuno-staining in MCF-7 cells

We synchronized MCF-7 cells in the G_1 phase using serum-starvation for 24 h. We then treated cells with etoposide (10 μM) for 30 min and IR, followed by washing and incubation with serum-free media. For the detection of FK2 and MRE11 foci, MCF-7 cells were permeabilized with TritonX-100 (0.5%) on ice for 10 min and then fixed with formaldehyde (4%) on ice for 15 min. For detection of RAP80 and γH2AX foci, the cells were fixed with paraformaldehyde (4%) on ice for 20 min and permeabilized with TritonX-100 (0.2%) on ice for 7 min. After incubation in blocking solution (5%) (BSA in PBS), the cells were incubated with the following primary antibodies for 1 h: α-FK2

(1/1000, MBL Life Science, Japan), α-BRCA1 (1/500, D-9, mouse monoclonal, Santa Cruz Biotechnology, US), α-RAP80 (1/1000, A300-763A, rabbit polyclonal, Bethyl Laboratories, US), α-γH2AX (1/1000, JBW301, mouse monoclonal, Millipore, US), α-γH2AX (1/500, 20E3, rabbit polyclonal, Cell Signaling Technology, US), α-CyclinA (1/500, EPR17351, rabbit polyclonal, Abcam, UK), α-53BP1 (1/1000, PC712, rabbit polyclonal, Merck, US) and α-MRE11 (1/500, 12D7, mouse monoclonal, GeneTex, US). After washing three times with PBS, cells were stained with α-mouse (Alexa Fluor 488), α-rabbit (Alexa Fluor 488), α-mouse (Alexa Fluor 594) or α-rabbit (Alexa Fluor 594) secondary antibodies. The slides were mounted in Fluoro-KEEPER containing 4', 6-diamidino-2-phenylindole (DAPI) (12745-74, Nacalai Tesque, Japan).

Focus counting and statistical analysis

For MCF-7 cells, foci images were captured using a BZ-9000 fluorescence microscope (Keyence). The number of the nuclear foci signals was automatically counted using Hybrid cell count software (Keyence). In TK6 cells, the number of nuclear foci counted by Hybrid cell count software was underestimated, because nuclei in TK6 cells are more round and thicker (~5 μm in diameter) in TK6 cell than that in adherent MCF-7 cells. To count all nuclear foci, 5 images at different focal planes through the entire thickness of the cellular nuclei were captured at 1 μm intervals along the Z-axis using confocal microscope (SP8, Leica, Germany). Image Z-stacks were projected using the maximal intensity method using LAS AF software (Leica, Germany). The number of γH2AX foci were counted blind. We performed all foci experiments independently at least three times for calculation of standard deviation and counted more than 50 cells at each experiment. The average foci numbers were counted from each experiment. The

bars in foci graphs indicate the average of average foci number from each experiment. The error bars indicate standard deviation calculated from average number of each experiment. The box plots in supplemental figures indicate the median (the line inside the box) and distribution of all foci (more than 150 dots in total) including more than three experiments.

Immunoprecipitation and western blotting

Whole-cell extracts were prepared from 5×10^6 cells lysed in IP buffer containing HEPES pH 7.5 (50 mM), KCl (150 mM), Tween 20 (0.05%), NP-40 (0.05%), Glycerol (10 %), NaF (2μM), Na_3VO_4 (0.4μM), Na-pyrophosphate (0.5 μM), 2 × protease inhibitor cocktail (5056489001, Complete, Roche, Switzerland), and β-glycerophosphate (2 μM). BRCA1 was immunoprecipitated with α-BRCA1 antibody (1/500, D-9, mouse monoclonal, Santa Cruz Biotechnology, US) pretreated with protein G magnetic beads (10004D, ThermoFisher, US). The magnetic beads were washed three times with IP buffer containing KCl (200 mM). The immunoprecipitates were subjected to SDS-PAGE and immunoblotting with α-BRCA1 and α-MRE11 (1/1000, 12D7, GeneTex, US). For signal detection, membranes were incubated with the appropriate HRP-linked secondary antibodies at room temperature for 1 h and developed by chemiluminescence using ECL reagent.

Trichloroacetic acid (TCA) precipitation

Cells (0.5×10^6 cells) were lysed in RIPA buffer containing Tris-HCl pH 7.6 (50 mM), NaCl (150 mM), NP-40 (1%), Sodium Deoxycholate (0.5%), and Sodium Dodecyl Sulfate (0.1%). The cellular lysates were precipitated with 20% TCA on ice for 30 min.

Centrifuge the samples at 13,000 g at 4 degree for 10min. Aspirate the supernatant and wash the pellets (ppts) with ice-cold acetone several times to completely remove the remaining TCA. The protein ppts were dissolved in 2 × Laemmli sample buffer and bailed for 10 minutes.

Construction of lentiviral plasmids expressing RAP80-WT and RAP80-UIMΔ

Wild-type RAP80 (RAP80-WT) gene and RAP80 (RAP80-UIMΔ) gene lacking UIM domain were amplified by PCR using the following primers from pSNAPf-RAP80-FLAG and pSNAPf-RAP80r-UIM-deletion (gifts from Dr. Shibata); the forward primer, 5'-CGGGTTTGCCGCCAGAACACAGGACCGGTATGGACTACAAAGACCATGA-3'; the reverse primer, 5'-TGTTTCAGCAGAGAGAAGTTTGTTGCGCCGGTGAATTCGAATTTTCTCC-3'. The amplified products were cloned into lentiCRISPRv2-Neo (Addgene#98292) digested with *Xba*I and *BamH*I by seamless reaction.

Construction of lentiviral plasmids expressing UBC13-WT and UBC13-C87A

UBC13 gene was amplified by PCR from a cDNA library using the following primers; the forward primer, 5'-GGGTTTGCCGCCAGAACACAGGACCGGTTATGGCCGGGCTGCCCCGCAG-3'; the reverse primer, 5'-TGTTTCAGCAGAGAGAAGTTTGTTGCGCCAATATTATTCATGGCATATAGC-3'. To generate shRNA-resistant UBC13 gene, we introduced silent mutations into UBC13 gene by PCR using the two primers, 5'-

GAAAGTAATGCTCGATACTTTTCATGTGGTCATTGCTGGCC-3' and 5'-

GATAAATTAGGTAGGATCTGCTTAGATATTTTGAAAGATAAG -3'.

To introduce the catalytic inactive mutation (C87A) of UBC13 gene, we used the

primer, 5'-GATAAATTAGGTAGGATCGCCTTAGATATTTTGAAAGATAAG-3'.

The amplified products were cloned into lentiCRISPRv2-Neo (Addgene#98292)

digested with *Xba*I and *BamH*I by seamless reaction.

SUPPLEMENTAL FIGURE LEGENDS

Figure S1 (related to Figure 1)

UBC13 contributes to DSB repair by recruiting BRCA1 and RAP80 onto DSB sites during the G$_1$ phase.

(A) Representative images of etoposide-induced FK2 and 53BP1 foci in asynchronous and serum-starved MCF-7 cells. Green specks indicate FK2 signal. The nuclei are outlined.

(B) Cell cycle analysis of serum-starved cells. Cells were incubated with serum-free medium for 24 h and stained with FITC-conjugated anti-BrdU antibody to measure BrdU incorporation into genomic DNA (y-axis, logarithmic scale) and with propidium iodide (PI) to measure the total DNA (x-axis, linear scale).

(C) Western blot analysis of *UBC13*-shRNA-treated (shUBC13) MCF-7 cells. Lanes 1 and 2 show *wild-type* MCF-7 and control-shRNA-treated cells, respectively, representing positive controls. Lanes 3-5 show a successful depletion of UBC13 by shRNA. β-Actin was a loading control.

(D) Distribution of etoposide-induced FK2 foci in shControl- and shUBC13-treated MCF-7 cells. Box plots display the median (black bars) and 25-75th percentiles (box ranges). A representative experiment (n=3, 150 cells) is shown. Single asterisk indicates $p < 2.2 \times 10^{-16}$, calculated by a Wilcoxon rank sum test.

(E) Western blotting analysis of γH2AX upon etoposide treatment. Serum-starved cells were incubated with etoposide (10 μM) for 30 min.

(F) Distribution of etoposide-induced γH2AX foci per cells in the indicated genotypes. Box plots indicate the median (bars), 25th, and 75th percentiles (boxes ranges). Single asterisks indicate $p < 2.2 \times 10^{-16}$, calculated by a Wilcoxon rank sum test.

(G) Schematic diagram of *DNA-PKcs* genomic locus, target location, and guide RNA (gRNA) sequence in MCF-7 cells.

(H) Western blots of the whole-cell extracts prepared from *wild-type* and *DNA-PKcs*$^{-/-}$ MCF-7 clones. β-Actin was a loading control.

(I and J) Distribution of BRCA1 (I) and RAP80 (J) foci per cell following 0.5-h pulse exposure to etoposide (10 μM) in individual MCF-7 cells (upper). Box plots display the median (black bars) and 25-75th percentiles (box ranges). Single and double asterisks indicate $p < 2.2 \times 10^{-16}$ and $p=5.0 \times 10^{-11}$, respectively calculated by a Wilcoxon rank sum test. A representative experiment (n=3, 150 cells) is shown. Green and red specks indicate BRCA1/RAP80 and γH2AX signals, respectively (lower). The nuclei are outlined.

(K) Western blotting analysis of RAP80 expression. The lenti-virus plasmids harboring *wild-type* RAP80-3FLAG and RAP80-ΔUIM-3FLAG (lacking UIM domain) were infected into *RAP80*$^{-/-}$ MCF-7 cells. The infected cells were selected in neomycin-containing medium. β-Actin was a loading control.

(L) Distribution (left graph) and representative images (right panels) of RAP80 foci per cell following 0.5-h pulse exposure to etoposide (10 μM) in individual MCF-7 cells. Box plots display the median (black bars) and 25-75th percentiles (box ranges). Single asterisk indicates $p < 2.2 \times 10^{-16}$ calculated by a Wilcoxon rank sum test. A representative experiment (n=3, 150 cells) is shown. Green and red specks indicate RAP80 and γH2AX signals, respectively. The nuclei are outlined.

Figure S2 (related to Figure 2)

RAP80 and BRCA1 contribute to DSB repair during the G$_1$ phase.

(A) Schematic diagram of *RAP80* genomic locus, target location, gene-targeting construct and guide RNA (gRNA) sequence in TK6 and MCF-7 cells. Targeting vectors having neomycin and puromycin were used only for the disruption of *RAP80* in TK6 cells.

(B) Western blotting analysis with α-RAP80 antibody to confirm the gene disruption events in the indicated genotypes. β-Actin was a loading control.

(C and D) The sensitivity of TK6 (C) and MCF-7 (D) cells to etoposide was measured by clonogenic cell-survival analysis. The dose for etoposide is displayed by the x-axis on a linear scale. The percentage of cell survival relative to that of untreated cells is shown by Y-axis on a logarithmic scale. Error bars show standard deviation (SD) calculated from three independent experiments.

(E and F) Distribution of γH2AX (E) and BRCA1 (F) foci per cell following pulse exposure (0.5 h) to etoposide (10 μM) in individual MCF-7 cells (upper). Box plots display the median (bars) and 25-75th percentiles (box ranges). Single asterisks indicate $p < 2.2 \times 10^{-16}$, calculated by a Wilcoxon rank sum test. A representative experiment (n=3, 150 cells) is shown. Representative images of etoposide-induced γH2AX (E) and BRCA1 (F) foci are shown (lower). Green specks indicate γH2AX (E) and BRCA1 (F) signals. The nuclei are outlined.

(G) Western blot analysis of BRCA1-shRNA-treated MCF-7 cells. Lanes 1 and 2 show *wild-type* MCF-7 and control-shRNA-treated cells, respectively. Lanes 3-5 show a successful depletion by shRNA in the indicated genotypes. β-Actin is a loading control.

(H) Distribution of γH2AX foci per cell following pulse exposure (0.5 h) to etoposide (10 μM) in individual MCF-7 cells (upper). A representative experiment (n=3, 150 cells) is shown. Box plots display the median (bars) and 25-75th percentiles (box

ranges). Single asterisks indicate $p < 2.2 \times 10^{-16}$, calculated by a Wilcoxon rank sum test. Representative images of etoposide-induced γH2AX foci are shown (lower). Green specks indicate γH2AX signals. The nuclei are outlined.

Figure S3 (related to Figure 3)

UBC13, RAP80, and BRCA1 promote the removal of etoposide-induced TOP2 adducts independent of TDP2.

(A) Schematic of *in vivo* TOP2cc measurement by immunodetection with α-TOP2 antibody.

(B) Degradation of BRCA1-mAID-GFP proteins two hours after exposure of *BRCA1$^{AID/AID}$* cells to auxin (250 nM). The whole-cell extracts were analyzed by western blot with α-BRCA1 antibody. β-Actin is a loading control.

(C) Schematic diagram of *RNF8* genomic locus, target location, and guide RNA (gRNA) sequence in TK6 cells (upper). Western blots of the whole-cell extracts prepared from *wild-type* and *RNF8$^{-/-}$* TK6 clones (lower). β-Actin was a loading control.

(D) Western blotting analysis of UBC13 expression. The lenti-virus plasmids harboring *wild-type* UBC13 (shUBC13-WT) and UBC13C87A (shUBC13-C87A, catalytic inactive form) were infected into UBC13-depleted MCF-7 cells. The infected cells were selected in puromycin-containing medium. β-Actin was a loading control.

(E, F, and G) Western blotting analysis of TOP2β in TK6 and serum-starved MCF-7 cells treated with etoposide (10 μM) ("+") or DMSO ("-") for 2 h.

Figure S4 (related to Figure 4)

K63 ubiquitin signaling involving UBC13, RAP80, and BRCA1 is required for efficient recruitment of MRE11 nuclease onto DSB sites in G$_1$ cells.

Representative images of MRE11 and 53BP1 foci following pulse-exposure (0.5 h) to etoposide. Green and red specks indicate MRE11 and 53BP1 signals, respectively. The nuclei are outlined.

Figure S5 (related to Figure 5)

Repair kinetics of *Asi*SI-induced DSBs and IR-induced DSBs in TK6 cells.

(A) Distribution of *Asi*SI-induced γH2AX foci in the indicated genotypes. Box plots display the median (bars) and 25-75th percentiles (box ranges). Single asterisks indicate $p < 2.2 \times 10^{-16}$, calculated by a Wilcoxon rank sum test. A representative experiment (n=3, 150 cells) is shown.

(B and C) Western blot analysis of UBC13-shRNA-treated (shUBC13) (B) and BRCA1-shRNA-treated (shBRCA1) (C) TK6 cells. Lanes 1 and 2 show *wild-type* and control-shRNA-treated (shControl) TK6 cells, respectively, representing positive controls. Lane 3 shows a successful depletion of UBC13 or BRCA1 by shRNA. β-Actin was a loading control.
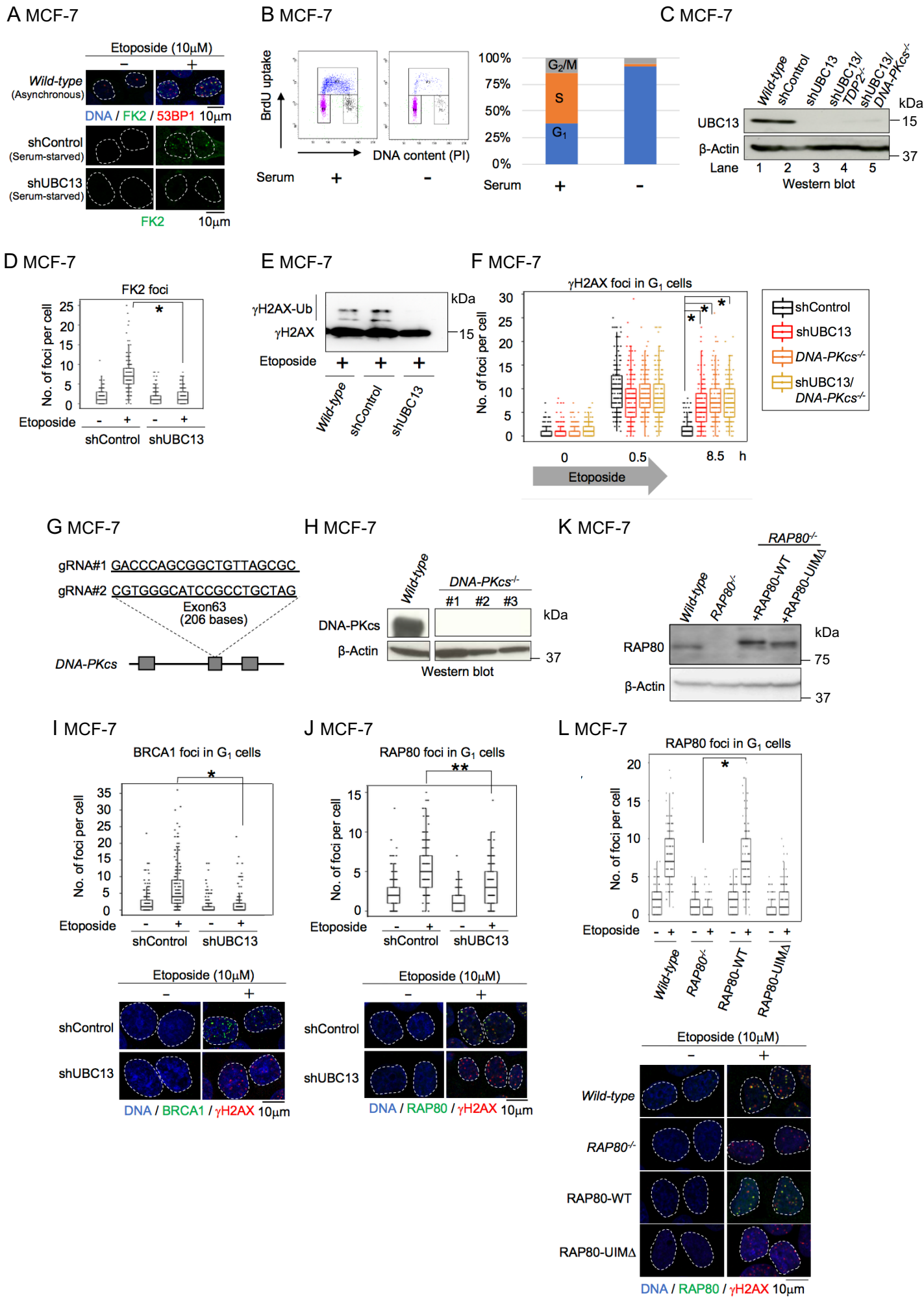
(D) Distribution of IR-induced γH2AX foci in the indicated genotypes. Box plots display the median (bars) and 25-75th percentiles (box ranges). Single asterisks indicate $p < 2.2 \times 10^{-16}$, calculated by a Wilcoxon rank sum test. A representative experiment (n=3, 150 cells) is shown.
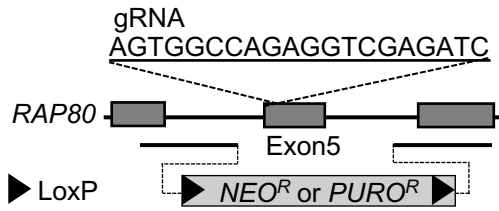
(E) Schematic diagram of *LIG4* genomic locus, gene-targeting construct, and gRNA sequence in TK6 cells (upper). Targeting events were confirmed by western blotting analysis (lower). β-Actin was a loading control.

(F) Distribution of IR-induced γH2AX foci in the indicated genotypes. Box plots display the median (bars) and 25-75th percentiles (box ranges). Single and double asterisks indicate $p = 1.9 \times 10^{-9}$ and p=5.1 × 10^{-8}, respectively calculated by a Wilcoxon rank sum test. A representative experiment (n=3, 150 cells) is shown.

(G) Western blot analysis of BRCA1-shRNA-treated (shBRCA1) TK6 cells. β-Actin was a loading control.

(H) Distribution of IR-induced γH2AX foci in the indicated genotypes. Box plots display the median (bars) and 25-75th percentiles (box ranges). Single and double asterisks indicate $p = 2.1 \times 10^{-12}$ and p < 2.2 × 10^{-16}, respectively calculated by a Wilcoxon rank sum test. A representative experiment (n=3, 150 cells) is shown.

Figure S6 (related to Figure 5)

Repair kinetics of IR-induced DSBs in *MRE11$^{AID/AID}$* HCT116 cells.

(A) Schematic diagram of *MRE11* genomic locus, gene-targeting construct, and gRNA sequence in HCT116 cells. "mAID" indicates the minimized sequence of the Auxin-induced-degron-tag. gRNA binds genomic sequences at the downstream of the termination codon of *MRE11* gene.

(B) Degradation of MRE11-mAID-GFP proteins two hours after exposure of *BRCA1$^{AID/AID}$* cells to auxin (250 nM). The whole-cell extracts were analyzed by western blot with α-MRE11 antibody. Ponceau staining was used to show equal loading.

(C) Western blotting analysis of MRE11-shRNA-treated (shMRE11) HCT116 cells. Lane 3 shows a successful depletion of UBC13 by shRNA. β-Actin was a loading control.

(D) Distribution of IR-induced γH2AX foci in the indicated cells. Box plots display the median (bars) and 25-75th percentiles (box ranges). Single asterisks indicate $p < 2.2 \times 10^{-16}$, calculated by a Wilcoxon rank sum test. A representative experiment (n=3, 150 cells) is shown.

Figure S7 (related to Figure 5)

Disruption of the genes encoding *POLβ*, *POLθ*, *TDP1*, *PARP1*, *ARTEMIS*, *EXD2*, and *EXO1* in TK6 cells and radiosensitivity of the resultant mutants.

(A-D and F-H) Schematic diagram of the genomic loci, target location, gene-targeting constructs and guide RNA (gRNA) sequences of the indicated genes in TK6 (upper). The targeting events were confirmed by western blotting, Southern blotting, and/or reverse transcription PCR (RT-PCR) analyses. β-Actin is a loading control for western blotting analysis. β-Actin and glyceraldehyde-3-phosphate dehydrogenase (GAPDH) are internal controls for RT-PCR analysis. Ponceau staining in (D) was used to show equal loading. Orange vertical and horizontal lines in (H) indicate *Hind*III restriction enzyme sites and probe for Southern blotting analysis, respectively.

(E) The doses that reduce percent colony survival to 50% (LD_{50}) following the exposure of the indicated genotypes to IR. Error bars represent SD of the mean from three independent experiments. The single, double, and triple asterisks indicate $p = 8.4 \times 10^{-3}$ (*Wild-type* vs. *EXD2$^{-/-}$*), $p = 7.8 \times 10^{-3}$ (*Wild-type* vs. *ARTEMIS$^{-/-}$*) and $p = 4.4 \times 10^{-3}$ (*Wild-type* vs. *EXO$^{-/-}$*), respectively, which were calculated by a Student's *t*-test.
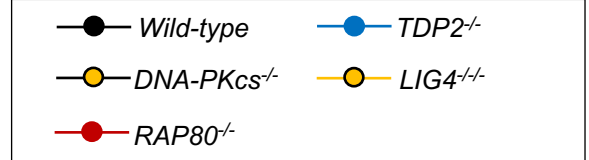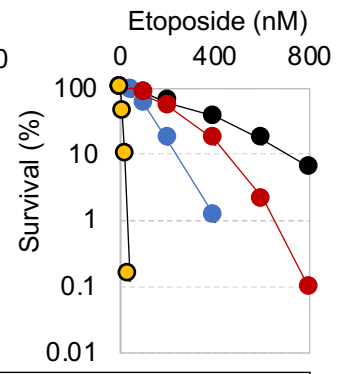
A TK6, MCF-7

gRNA
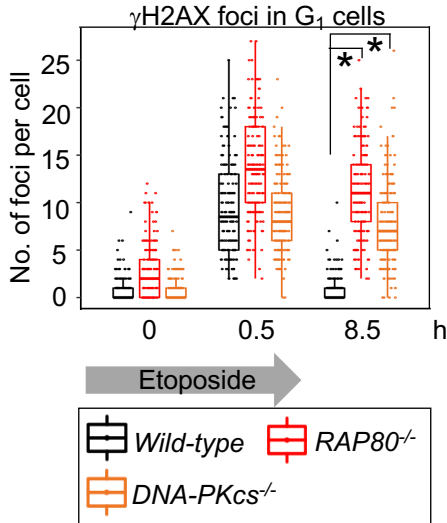AGTGGCCAGAGGTCGAGATC

RAP80

Exon5

▶ LoxP

NEO^R or *PURO^R*

B TK6, MCF-7

RAP80
β-Actin

Wild-type / RAP80^-/- / RAP80^-/-/TDP2^-/-
#1 #2 #1 #2

Wild-type / RAP80^-/-
#1 #2

MCF-7   TK6

Western blot

C TK6

Etoposide (nM)

Survival (%)

D MCF-7

Etoposide (nM)

Survival (%)

● *Wild-type*   ● *TDP2^-/-*
● *DNA-PKcs^-/-*   ● *LIG4^-/-/-*
● *RAP80^-/-*

E MCF-7

γH2AX foci in G₁ cells

No. of foci per cell

Etoposide

□ *Wild-type*   □ *RAP80^-/-*
□ *DNA-PKcs^-/-*

F MCF-7

BRCA1 foci in G₁ cells

No. of foci per cell

Wild-type   *RAP80^-/-*   *Wild-type*   *RAP80^-/-*

−   +

Etoposide

H MCF-7

γH2AX foci in G₁ cells

No. of foci per cell

Etoposide

□ shControl   □ *DNA-PKcs^-/-*
□ shBRCA1   □ shBRCA1/*DNA-PKcs^-/-*

Etoposide (10μM)
0 h   8.5 h

Wild-type
DNA-PKcs^-/-
RAP80^-/-

DNA / γH2AX / CyclinA   10μm

Etoposide (10μM)
−   +

Wild-type
RAP80^-/-

BRCA1   10μm

Etoposide (10μM)
0 h   8.5 h

shControl
DNA-PKcs^-/-
shBRCA1
shBRCA1/*DNA-PKcs^-/-*

DNA / γH2AX / CyclinA   10μm

G MCF-7

BRCA1
β-Actin

Wild-type / shControl / shBRCA1 / shBRCA1/DNA-PKcs^-/- / shBRCA1/TDP2^-/-

kDa
250

37

Lane   1   2   3   4   5

MCF-7

Etoposide (10μM)

| | − | + |

Wild-type

shControl

shUBC13

shBRCA1

RAP80^{-/-}

DNA / MRE11 / 53BP1   10μm

A HCT116

gRNA
CTGAGAAACATGCAAGATAC

Termination codon

MRE11

Left arm   Right arm

MRE11^{AID/AID}

► LoxP	⟹ Marker	Homologous region
Exon	mAID	GFP
PolyA		

B HCT116

MRE11^{AID/AID}

Auxin   −   +   kDa

MRE11-mAID-GFP   Western blot

— 100

— 80   Ponceau staining

C HCT116

Wild-type   shMRE11   kDa

MRE11   — 75

β-Actin   — 37

Western blot

D HCT116

γH2AX foci in G$_1$ cells

No. of foci per cells

Time after IR (h)

⊟	*Wild-type*
⊟	*DNA-PKcs* inhibitor
⊟	*MRE11^{AID/AID}* (−Auxin)
⊟	*MRE11^{AID/AID}* (+Auxin)
⊟	shMRE11
⊟	shMRE11 +*MRE11^{AID/AID}* (+Auxin)

A TK6

gRNA
GGAATCACCGACATGCTCAC

POLβ
Exon 1
▶LoxP   Marker

POLβ — 925 bp

β-Actin — 925

Wild-type   *POLβ⁻/⁻*

RT-PCR

B TK6

gRNA#2
GCAGTGTGCGACTGTGATAC

gRNA#1
CAGTTCAGATGACATCGCTG

POLθ
Exon 21
▶LoxP   Marker

POLθ — 925 bp
ACTN1 — 925

Wild-type   *POLθ⁻/⁻* #1 #2

RT-PCR

C TK6

gRNA
GCAAAGTTGGATATTGCGTT

TDP1
Exon 7
* Catalytic site
▶LoxP   Marker

TDP1 — 75/50 kDa
TDP2 — 50/37
β-Actin — 37

Wild-type *TDP1⁻/⁻* *TDP2⁻/⁻* *TDP1⁺/⁻/TDP2⁻/⁻*

Western blot

D TK6

gRNA
AAGTACGTGCAAGGGGTGTA

PARP1
Exon 3
▶LoxP   Marker

PARP1 — 100 kDa   Western blot
— 100   Ponceau staining
— 37

Wild-type   *PARP1⁻/⁻*

E TK6

IR, LD₅₀ (Gy)

EXD2⁻/⁻   *
ARTEMIS⁻/⁻   **
POLθ⁻/⁻
TDP1⁻/⁻/TDP2⁻/⁻
XRCC1⁻/⁻
PARP1⁻/⁻
EXO1⁻/⁻   ***
POLβ⁻/⁻
Wild-type

0   Gy   1

F TK6

gRNA
#1, TCTCCATAGACCGCTTCGAT
#2, TAGACCGCTTCGATAGGGAG
#3, GAGGGCCCGCGCCTACTTCC

ARTEMIS
Exon 1
▶LoxP   Marker

ARTEMIS — 200 bp
GAPDH — 200

Wild-type   *ARTEMIS⁻/⁻* #1 #2 #3

RT-PCR

G TK6

gRNA
#1, AAAATATCCAATAACGTTCT
#2, AGGATTATGGCCTCGTTGTT

EXD2
Exon 3
▶LoxP   Marker

EXD2 — 500 bp
GAPDH — 200

Wild-type   *EXD2⁻/⁻* #1 #2

RT-PCR

H TK6

gRNA
TCAGGGGGTAGATTGCCTCG

EXO1
Exon 5
▶LoxP   Marker

— 6.6 kbp
— 2.3

Wild-type   *EXO1⁻/⁻* #1 #2

Southern blot